# Retrieving surface soil moisture at high spatio-temporal resolution from a synergy between Sentinel-1 radar and Landsat thermal data: A study case over bare soil

Abdelhakim Amazirh, Olivier Merlin, Salah Er-Raki, Qi Gao, Vincent Rivalland, Yoann Malbéteau, Said Khabba, Maria-José Escorihuela

# Retrieving surface soil moisture at high spatio-temporal resolution from a synergy between Sentinel-1 radar and Landsat thermal data: a study case over bare soil

**Abdelhakim Amazirh[1,2,*], Olivier Merlin[2,5], Salah Er-Raki [1], Qi Gao[3,2], Vincent Rivalland[2], Yoann Malbeteau[2,4], Said Khabba[5], Maria José Escorihuela[3]**

[1] LP2M2E, Département de Physique Appliquée, Faculté des Sciences et Techniques, Université Cadi Ayyad, Marrakech, Morocco

[2] CESBIO, Université de Toulouse, CNES/CNRS/IRD/UPS, Toulouse, France :

[3] isardSAT, Parc Tecnològic Barcelona Activa, Carrer de Marie Curie, 8, 08042 Barcelona, Spain.

[4] Water Desalination and Reuse Center, King Abdullah University of Science and Technology, Thuwal, Saudi Arabia.

[5] LMME, Département de Physique, Faculté des Sciences Semlalia, Université Cadi Ayyad, Marrakech, Morocco.

# Abstract

Radar data have been used to retrieve and monitor the surface soil moisture (SM) changes in various conditions. However, the calibration of radar models whether empirically or physically-based, is still subject to large uncertainties especially at high-spatial resolution. To help calibrate radar-based retrieval approaches to supervising SM at high resolution, this paper presents an innovative synergistic method combining Sentinel-1 (S1) microwave and Landsat-7/8 (L7/8) thermal data. First, the S1 backscatter coefficient was normalized by its maximum and minimum values obtained during 2015-2016 agriculture season. Second, the normalized S1 backscatter coefficient was calibrated from reference points provided by a thermal-derived SM proxy named soil evaporative efficiency (SEE, defined as the ratio of actual to potential soil evaporation). SEE was estimated as the radiometric soil temperature normalized by its minimum and maximum values reached in a water-saturated and dry soil, respectively. We estimated both soil temperature endmembers by using a soil energy balance model forced by available meteorological forcing. The proposed approach was evaluated against *in situ* SM measurements collected over three bare soil fields in a semi-arid region in Morocco and we compared it against a classical approach based on radar data only. The two polarizations VV (vertical transmit and receive) and VH (vertical transmit and horizontal receive) of the S1 data available over the area are tested to analyse the sensitivity of radar signal to SM at high incidence angles (39°-43°). We found that the VV polarization was better correlated to SM than the VH polarization with a determination coefficient of 0.47 and 0.28, respectively. By combining S1 (VV) and L7/8 data, we reduced the root mean square difference between satellite and *in situ* SM to 0.03 $m^3$ $m^{-3}$, which is far smaller than 0.16 $m^3$ $m^{-3}$ when using S1 (VV) only.



*Keywords: near surface soil moisture, Sentinel-1 (A/B), Landsat-7/8, energy balance modelling, soil evaporation, bare soil.*


# 1. Introduction

Soil moisture plays a very important role in many domains, such as agriculture, hydrology and meteorology. Consequently, the development of innovative techniques to monitor this variable from space becomes crucial. Remote sensing has demonstrated a strong potential for estimating the surface soil moisture (SM) in the first cm of soil (Bruckler et al., 1988; Du et al., 2000; Engman, 2000) while SM can be estimated using optical/thermal data (Gillies and Carlson, 1995; Sandholt et al., 2002). Several studies have generally acknowledged that microwave techniques have a higher potential for retrieving SM on a regular basis, either from active (Dubois and Engman, 1995a; Ulaby et al., 1979, 1978; Zribi et al., 2005; Zribi and Dechambre, 2003) or passive (Kerr et al., 2010; Entekhabi et al., 2010) sensors.

Microwave methods are based on the large difference existing in the dielectric constant between a dry soil (around 4) and that of water, which is around of 80 at microwave frequencies (Ulaby et al., 1986). Radiative transfer models have hence been developed based on the SM-dielectric constant relationship (Dobson et al., 1985).

In the recent past, the use of imaging radar to estimate SM has become a subject of strong interest, notably due to i) the high-spatial resolution achievable by synthetic aperture radars (SAR) and ii) the advent of SAR data available at high-temporal resolution. Especially, the Sentinel-1 (S1) constellation (composed of two satellites S1-A and S1-B) potentially provides SAR data at 20 m resolution every 3 days (Torres et al., 2012). Thus, numerous studies have investigated and exploited the sensitivity of the radar signal to SM (Baghdadi et al., 2002a; Baghdadi and Zribi, 2006; Fung, 1994; Holah et al., 2005a; Oh et al., 1992; Srivastava et al., 2003; Ulaby et al., 1986; Van Oevelen and Hoekman, 1999; Vereecken et al., 2008; Zribi et al., 2005). Retrieval approaches can be categorized into i) purely empirical modelling approaches (Baghdadi et al., 2002a; Holah et al., 2005; Mathieu et al., 2003; Wickel et al., 2001; Baghdadi et al., 2016) without any physical basis, which makes them valid for the studied area solely, and ii) semi-empirical approaches (Attema and Ulaby, 1978; Dubois and Engman, 1995a; Oh, 2004; Oh et al., 1992; Shi et al., 1997), which usually combine empirical (data fits) and theoretical (physically-based) models like integral equation model (IEM) (Fung et al., 1992). In general, each model has a certain validity range in terms of observation incidence angle, soil parameters and vegetation cover (Fung et al., 1992; Karam et al., 1992).

Models, previously mentioned, do not reach the expected accuracy in SM retrievals (Alexakis et al., 2017; Bai et al., 2017; Fieuzal et al., 2011; Gao et al., 2017; Rakotoarivony L. et al., 1996; Remond et al., 1999; Zribi et al., 1997). This is owing to the various radar (incidence angle, frequency and polarization) and surface (soil moisture and roughness) parameters that affect the behaviour of the backscattered signal. The surface roughness is one of the most important factors that impact on the SM estimation, and probably the most difficult to measure periodically when monitoring SM changes over wide areas (Loew et al., 2006). Usually, the use of such models requires a calibration step to reduce discrepancies between simulated backscatter coefficient (or inverted SM) and reference (measured) SM. Calibration is often performed using *in situ* SM measurements (Dubois and Engman, 1995b; Oh, 2004; Oh et al., 1992). In this vein, various research studies have focused on the calibration of the IEM (Baghdadi et al., 2006, 2011, 2004, 2002b; Susaki, 2008), in which *in situ* SM measurements have been used to invert the local roughness (autocorrelation length and standard deviation of surface height). However, calibrating IEM over large areas is not a trivial issue due to the lack of available *in situ* measurements. Moreover, the surface roughness generally changes over time, which makes the autocorrelation length and the standard deviation of surface height quite difficult to estimate accurately. Because of uncertainties in the estimation of roughness

parameters and thus in the modelling of soil roughness, discrepancies may remain between inverted and *in situ* SM. Regarding this point, Srivastava et al. (2009) proposed a practical methodology to decouple the effect of surface roughness in soil moisture estimation, without any assumption or prior knowledge of surface roughness distribution, exploiting multi-incidence-angle radar data. Note that the retrieval model parameters were calibrated using soil moisture truth measurements.

Alternatively to microwave approaches, thermal remote sensing has also been extensively used to monitor SM (Friedl and Davis, 1994; Gillies and Carlson, 1995; Qin et al., 2013; Schmugge, 1978) and SM-related variables such as evapotranspiration (Choi et al., 2011; Desborough et al., 1996; Entekhabi et al., 1996; Verstraeten et al., 2008). The land surface temperature (LST) derived from the thermal domain, is coupled to SM via the energy balance equation when the incoming energy is not limiting. As demonstrated in Price (1990), Carlson (2007), Carlson et al. (1995), Moran et al. (1992), Smith and Choudhury (1991) and Gao et al. (2017), LST and vegetation index (VI) can provide SM information by interpreting the spatial distribution of data pixels spatial distribution in the LST-VI feature space delimited by a triangle or a trapezoid. This has been the basis for developing thermal-derived SM proxies. McVicar et al. (1992) developed the normalized difference temperature index (NDTI) using the upper and lower boundary conditions for LST, which were simulated by an energy balance model forced by atmospheric forcing data. The spatio-temporal variations in NDTI and SM ground measurements were found to be consistent. Other indexes have been proposed which help to estimate SM using the trapezoid method (Zhang and Zhou, 2016), such as the crop water stress index (CWSI, Jackson and Pinter, 1981), water deficit index (WDI, Moran et al., 1994) and temperature–vegetation dryness index (TVDI, Sandholt et al., 2002). Zhang et al. (2014) recently argued that TDVI is an ideal proxy to retrieve SM. Such thermal-derived SM proxies have also been extensively used to downscale global scale microwave-derived SM products (Molero et al., 2016; Peng et al., 2017). In addition, recent works about the synergy between microwave and optical data, have demonstrated the potential to retrieve surface SM including the effect of vegetation (Gao et al., 2017; Mattar et al., 2012; Santamaria-Artigas et al., 2016). However, both radar- and thermal-based SM retrieval approaches have inherent limitations. while, the radar backscatter is highly sensitive to surface roughness effects and to the structure of vegetation canopy, thermal data are unavailable under cloudy conditions and may be weakly linked to SM when the incoming energy is limiting (e.g. during the night and when the evaporative demand is low) or over densely vegetated surfaces. Hence the idea to combine radar- and thermal-based approaches is to benefit from the advantages of i) all-weather and day/night capabilities of microwave sensors, and ii) the physical basis of the LST-SM relationship that occurs via the surface energy budget under relatively large evaporative demand conditions.

In this context, the overall objective of the present paper is to develop a new methodology to retrieve SM from Sentinel-1 (S1) C-band microwave (MW) and Landsat-7/8 (L7/8) thermal data, by taking advantage of the high spatio-temporal resolution of S1 and by building on the synergy between radar and LST data. The approach was tested over bare agricultural fields in the semi-arid Tensift/Marrakech area during the 2015-2016 agricultural season.

# 2. Data and study area description

## 2.1 Studied area

The studied sites are located east of Marrakech in the semi-arid Tensift watershed (20 450 $km^2$ of size) in central Morocco (Figure 1). Within this region, about 85% of available water is used for agriculture, where wheat crops are dominant (Duchemin et al., 2006; Er-Raki et al., 2007; Hadria et al., 2006; Kharrou et al., 2013). Reference evapotranspiration ($ET_0$) is about 1600 $mm.year^{-1}$ while rainfall is about 250 $mm.year^{-1}$, leading to irrigation and increasing concerns related to optimizing the management of water resources. In this context, numerous studies have been carried out since 2002 on this area (Amazirh et al., 2017; Chehbouni et al., 2008; Jarlan et al., 2015; Khabba et al., 2013).

Three experimental fields were selected: a 1 ha rainfed wheat field (Sidi Rahal site, 31° 42′03″ N, 7° 21′ 08″ E, 767 m), and two 3 ha wheat fields located in the irrigated zone named R3. All the three sites had remained under bare soil conditions during the 2015-2016 agricultural season. Based on soil analyses performed at the sites (Er-Raki et al., 2007), soil texture is sandy (18% clay) and clayey (47% clay) for Sidi Rahal and R3 fields, respectively.

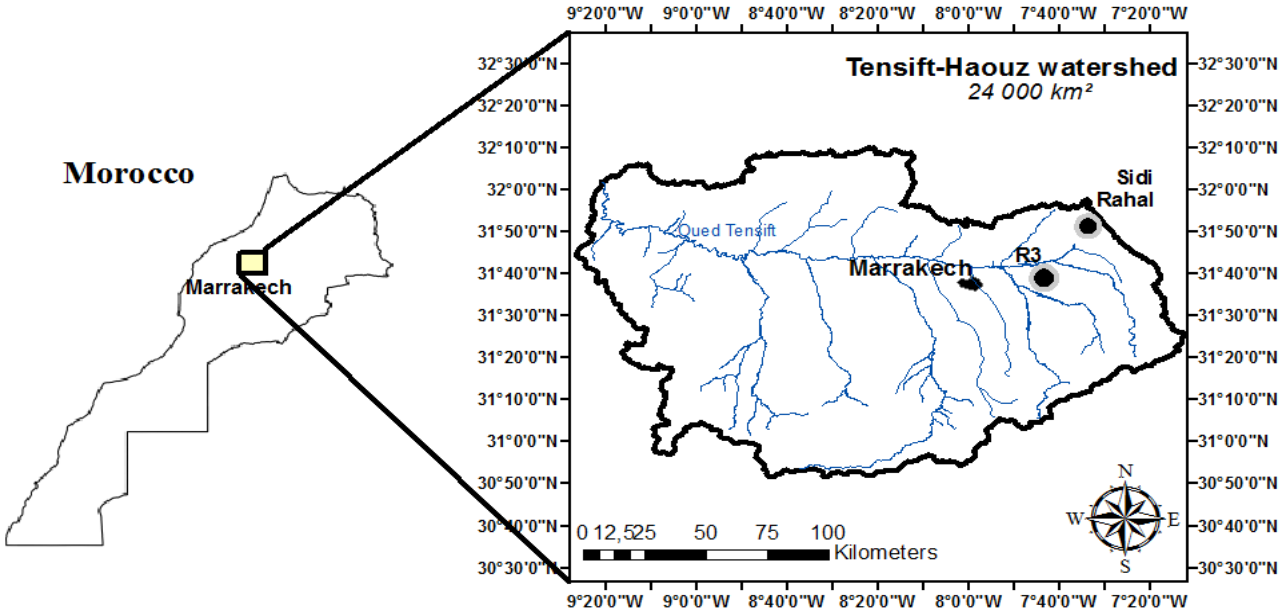


*Figure1: Location of the R3 and Sidi Rahal study sites (black circles).*

## 2.2 Remote sensing data

Remote sensing data used in this study are acquired by two sensors: Landsat L7/L8 and Sentinel1 A/B. Table 1 summarises the characteristics of S1 radar and L7/L8 sensors for SM retrieval at high (100 m and finer) spatial resolution.

*Table 1: S1 radar and L7/8 optical sensors characteristics.*

| Sensors/Mission | Characteristics | Advantages for SM retrieval | Limitations for SM retrieval |
|---|---|---|---|
| **S1 A/B** | 5.405 GHz (C-band), HH-HV and VV-VH polarizations, 4/8-day repeat cycle (S1B has a 6-day offset from S1A), overpass time at 06:30 AM (descending) and 06:30 PM (ascending) | High spatial (20 m) and temporal (potentially 3 days) resolution<br>All weather capabilities | Highly influenced by surface roughness and speckle |
| **L7/8** | Multiband, 16-day repeat cycle (L8 has a 8-day offset from L7), overpass time at 11:30 AM | High spatial resolution (60 m to 100 m for thermal data) and multi-band data available in the shortwave domain;<br>LST is related to SM through the physical energy balance equation | Relatively low temporal (8 days) resolution;<br>Highly sensitive to meteorological conditions (including night effects);<br>Cloud masking |

### 2.2.1 Landsat data

We have collected data from two thermal infrared (TIR) missions: L7 that provides a single band in the TIR domain (band 6, 10.40-12.50 µm) with a spatial resolution of 60m, and L8 that provides two thermal bands (10.60-11.19 µm and 11.50-12.51 µm for bands 10 and 11) with a spatial resolution of 100 m. L7 and L8 were launched by NASA in April 1999 and February 2013, respectively. The L8 satellite is equipped with multispectral sensors including: 1) Operational Land Imager (OLI) that acquires imagery in nine spectral bands ranging from visible to medium infrared with 7 bands already existing on L7 (two channels were added on L8 for cloud detection and atmospheric correction) and 2) Thermal Infrared Sensor (TIRS), which provides TIR bands at a 100 m spatial resolution (60 m for the L7 TIR band). The revisit time is 16 days for both satellites and L8 has an 8-day offset from L7, so the combination of both platforms potentially provides TIR data (in clear sky conditions) every 8 days globally.

In this study, Landsat data were downloaded from the USGS website (http://earthexlorar.com/), were resampled to 30 m resolution and were projected using the Universal Transverse Mercator (UTM), Zone 29N, World Geodetic System (WGS) 84 coordinate system. The images were acquired between 01 January 2016 and 10 October 2016 for the Sidi Rahal site (23 cloud free images) and from 01 January to 18 May 2016 for the R3 sites (11 cloud free images).

To obtain the actual LST from Landsat thermal radiance, we followed the correction steps described in Tardy et al, (2016): i) Converting digital numbers (DN) to top-of-the-atmosphere (TOA) radiance values. ii) Correcting (TOA) radiance from atmospheric effects in the sun-target-sensor path using the spectral atmospheric transmission and the atmospheric downwelling and upwelling radiances. The atmospheric parameters are modelled using the MODTRAN atmospheric radiative transfer model (Berk et al., 2005). The atmospheric profile composition (vertical air temperature and water content) needed as input to the model is obtained from the ECMWF European Reanalysis (ERA) Interim product (Dee et al., 2011). iii) Estimating the surface emissivity using an empirical relationship (Tardy et al., 2016) based on the normalized difference vegetation index (NDVI). NDVI is calculated using the Landsat red and near-infrared bands. Emissivity varies between 0.95 (bare soil) and 0.99 (full vegetation). iv) Calculating LST using the simplified Plank's law (Equation 1). The derived spectral atmospheric parameters and the surface emissivity permit the conversion of the at-sensor radiance into top of canopy radiance (TOC) exempt from atmospheric effects.

$$LST = \frac{K_2}{\ln\left(\frac{K_1}{B_{TOC(T)}}+1\right)} \quad (1)$$

where $K_1$, and $K_2$ are the band-specific thermal conversion constants provided by the USGS and $B_{TOC}$ the TOC spectral radiance of ground surface.

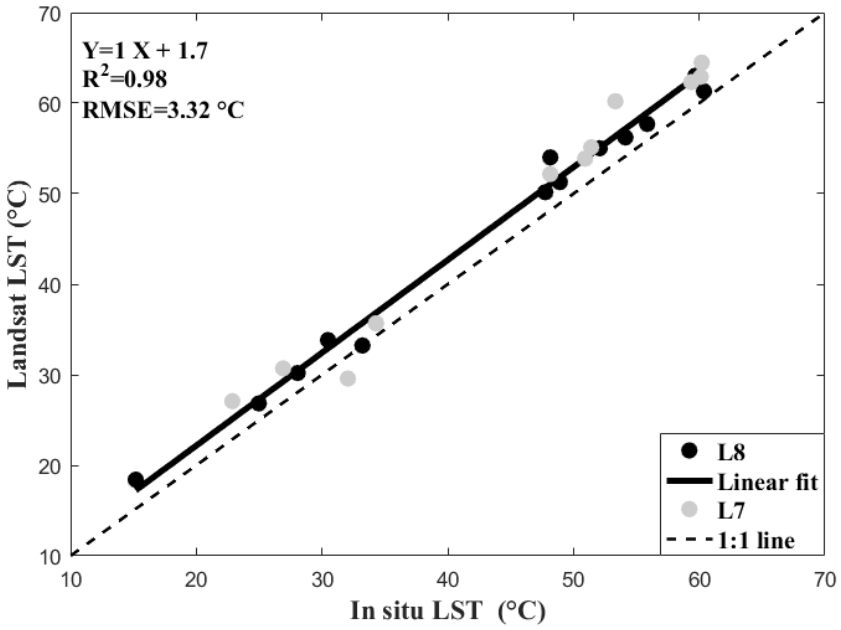


*Figure 2: LST derived from Landsat-7 and -8 versus in situ measurements for Sidi Rahal site.*

In order to assess the reliability of LST remote sensing data derived from L7/8, the extracted Landsat LST is then aggregated at the field scale, and a comparison between the aggregated Landsat and *in situ* LST is presented in Figure 2 for Sidi Rahal site. A satisfying match is observed between *in situ* and satellite LST with a $R^2$ (determination coefficient) of 0.98 and a RMSE (root mean square error) equal to 3 °C. The slight overestimation of Landsat LST could be attributed to the lack of spatial representativeness of *in situ* data at the L7/8 pixel scale, and this is consistence with the work of Amazirh et al., (2017) when comparing L7/8 and *in situ* LST for drip and flood irrigated sites. Note that the soil emissivity is difficult to estimate without specific measurements, which were unavailable in this experiment. The soil emissivity was hence fixed to a typical value (0.95) for agricultural soils. A sensitivity analysis (results not shown) indicates that changing the soil emissivity from 0.95 to 0.98 slightly impacts the LST estimations (an error difference of 0.32 °C) and has no significant effect on the retrieved SM. Note that large LST values (up to 60 °C) were acquired during the summer over the bare soil (Sidi Rahal) site.

### 2.2.2 Sentinel-1 data

The S1 radar sensor operates at C-band (frequency 5.33 GHz, wavelength 5.6 cm). S1 A and B satellites were launched by the European Space Agency (ESA) in the frame of Europe's Copernicus programme in 2014 and 2016 respectively. Both satellites orbit the whole earth at an altitude of ~700 km sharing the same orbital plane with a 180° orbital phasing difference.

Level 1 S1 products were downloaded from the Sentine-l Data Hub website (https://scihub.copernicus.eu/). 45 S1 images were acquired for Sidi Rahal site and 23 images over the R3 area. The incidence angle (~40°)

of S1 observations is about the same for both Sidi Rahal and R3 sites for ascending and descending overpasses. S1 operates at different modes acquiring images in different combinations of polarization depending on the transmitted and received signals and at different resolutions. Over land S1 operates in Interferometric Wide Swath mode providing data at the cross polarization VH (vertical-horizontal) and co-polarization VV (vertical-vertical) mode at a spatial resolution of about 20m.

Data processing of the level 1 data products consisted in: i) Removing thermal noise by subtracting the additive noise from the power-detected image. The disturbing additive thermal noise (mostly in the lower range of backscatter intensity values) was removed using the calibrated noise vectors provided by ESA. ii) Computing the backscatter coefficient by calibrating the physical backscatter using the sensor calibration parameters provided by ESA in the GRD (Ground range Detected) metadata. iii) Correcting the backscatter coefficient for terrain and geometric effects to reduce the effects of shadow, folding and contraction on the radar signal, also to convert the Ground Range Multi-Look Detected (GRD) products, which do not take into account terrain elevation. The 30 m resolution SRTM (Shuttle Radar Topography Mission) was used as a DEM (Digital Elevation Model). iv) Filtering speckle effects to reduce random uncertainties related to the coherence interference of the waves reflected from the many elementary scatters. Images were filtered using the 5x5 refined Lee speckle filter described in Lee et al, (1994) and Lee (1999).

The mean backscatter radiation (linear units) is calculated from previously calibrated S1 images, and converted to decibel (dB) using the formula:

$$\sigma^{\circ}\ (\mathrm{dB}) = 10 \log_{10} (\sigma^{\circ}) \qquad (2)$$

Consistent with LST and *in situ* SM data, the backscatter coefficient was aggregated (average) in linear units before conversion to decibel at the crop field scale for each site.

## 2.3 Ground data

At the Sidi Rahal site an eddy covariance station has been monitoring the four components of the energy balance since 2013. The latent and sensible heat fluxes were estimated using a Hygrometer KH20 and an anemometer CSAT3. The net radiation was measured by CNR1, and ground conduction flux estimated using HFP01 plates buried at a 5-cm depth. SM is continuously measured using time domain reflectometer probes (CS616) installed at different depths (5, 10, 20, 30, 50, 70 cm). The radiometric LST was measured by an Apogee 8-14 µm thermal radiometer sensor looking at nadir, set up at a 2-m height.

For both R3 fields, the near-surface (0-5 cm) SM was measured within ±2 h of the L7/8 and S1 satellites overpasses using a frequency domain sensor (Theta probe) at 5 locations on both sides of each field. For each sampling date and field, an average of the 10 measurements was computed to reduce uncertainties in

field-scale SM estimates. Soil samples over a 0 to 5 cm depth were also taken over both sites in order to calibrate Theta probe measurements using the gravimetric technique.

S1 and L7/8 never overpass the study area on the same day. However, Table 2 lists the dates with quasi-concurrent (one day offset) L7/8/S1 overpasses. In the R3 area i*n situ* SM sampling were undertaken on those particular dates, either on S1 and L7/L8 overpass date, or on both successive dates. The SM sampling dates are also reported in Table 2. The consistency of the SM data collected on two successive dates was checked (results not showed). Both SM data sets were consistent with a root mean square difference of 0.02 $m^3$ $m^{-3}$, except when an irrigation or a rainfall event occurred between sampling dates. Those particular dates were removed from the data set.

*Table 2: Dates with quasi concurrent L7/8/S1 overpasses used in the analysis for both study sites.*

| Date (mm/dd-dd/yyyy) | S1 overpass Time (UTC) | Study Site | Thermal sensor | S1 orbit | R3 SM sampling |
|---|---|---|---|---|---|
| **01/06-07/2016** | 06:30 am | Sidi Rahal | L8 | Ascending | No* |
| **01/14-15/2016** | 06:30 pm | Sidi Rahal /R3 | L7 | Descending | Yes |
| **01/30-31/2016** | 06:30 am | Sidi Rahal /R3 | L7 | Ascending | Yes |
| **02/07-08/2016** | 06:30 pm | Sidi Rahal /R3 | L8 | Descending | Yes |
| **02/23-24/2016** | 06:30 am | - | L8 | Ascending | No* |
| **03/02-03/2016** | 06:30 pm | Sidi Rahal /R3 | L7 | Descending | Yes |
| **03/18-19/2016** | 06:30 am | R3 | L7 | Ascending | Yes |
| **03/26-27/2016** | 06:30 pm | R3 | L8 | Descending | Yes |
| **04/11-12/2016** | 06:30 am | - | L8 | Ascending | No* |
| **04/19-20/2016** | 06:30 pm | Gap fil** | L7 | Descending | Yes |
| **05/05-06/2016** | 06:30 am | R3 | L7 | Ascending | Yes |
| **05/13-14/2016** | 06:30 pm | - | L8 | Descending | No* |
| **05/29-30/2016** | 06:30 am | Sidi Rahal | L8 | Ascending | - |
| **06/06-07/2016** | 06:30 pm | Sidi Rahal | L7 | Descending | - |
| **06/22-23/2016** | 06:30 am | Sidi Rahal | L7 | Ascending | - |
| **06/30-07/01/2016** | 06:30 pm | Sidi Rahal | L8 | Descending | - |
| **07/16-17/2016** | 06:30 am | Sidi Rahal | L8 | Ascending | - |
| **07/24-25/2016** | 06:30 pm | Sidi Rahal | L7 | Descending | - |
| **08/09-10/2016** | 06:30 am | Sidi Rahal | L7 | Ascending | - |
| **08/17-18/2016** | 06:30 pm | Sidi Rahal | L8 | Descending | - |
| **09/02-03/2016** | 06:30 am | - | L8 | Ascending | - |
| **09/10-11/2016** | 06:30 pm | Sidi Rahal | L7 | Descending | - |
| **09/26-27/2016** | 06:30 am | - | L7 | Ascending | - |
| **10/04-05/2016** | 06:30 pm | Sidi Rahal | L8 | Descending | - |

**: cloudy day*

***: the Landsat-7 images include data gaps due to scan line corrector failure on May 31, 2013, which on this date unfortunately covered our sites.*

Meteorological forcing was continuously monitored at the 30 min step in the R3 area using an automatic meteorological weather station set up over a grass cover: wind speed $u_a$ measured by CSAT3 sonic Anemometer, solar radiation $R_g$ measured by pyranometer and air temperature $T_{air}$ and relative humidity $rh_a$ measured by a HMP155 probe at a reference height of 2 m.

# 3. Soil moisture retrieval approaches

Retrieving SM from radar data implies establishing a relationship between the volumetric SM and the backscatter coefficient (σ°) obtained from SAR data. Over bare soil surfaces, the VV and VH polarized backscatter signal depends of SM, surface roughness and the observation configuration mainly defined by the incidence angle and microwave frequency (Lievens and Verhoest, 2011). As a first approximation, a linear relationship can be established as following (Champion and Faivre, 1997; Dobson and Ulaby, 1986; Holah et al., 2005; Le Hégarat et al., 2002; Ulaby et al., 1979):

$$SM = SM_{min} + (SM_{max} - SM_{min}) \times SMP \quad (3)$$

where SMP is a radar-based SM proxy (function of σ°) and $SM_{min}$ and $SM_{max}$ the minimum and maximum SM values depending mainly on the soil porosity (Brisson and Perrier, 1991; Cosby et al., 1984).

As previously mentioned, we proposed a method to integrate the thermal data extracted from L7/L8 data into a S1-based retrieval approach. The performance of the radar/thermal combining approach was evaluated by comparing it to a benchmark approach based on radar only. The two (benchmark and combined radar/thermal) methods for estimating SMP and the SM endmembers of Equation (3) are presented in the schematic diagram of Figure 3 and are described below.

## 3.1 Benchmark approach: Based only on radar data

SMP of Equation (3) is expressed as in Fieuzal (2010) and Wagner et al. (1999a):

$$SMP_{\sigma} = \left(\frac{\sigma^0_{pp} - \sigma^0_{pp,min}}{\sigma^0_{pp,max} - \sigma^0_{pp,min}}\right) \quad (4)$$

with $\sigma^0_{pp,max}$ and $\sigma^0_{pp,min}$ being the maximum and minimum backscatter coefficient, respectively and p=V (Vertical) or H (Horizontal).

As in Omer et al. (2015) and Wagner et al. (1999b), the minimum SM value is set to the residual SM, which can be related to clay fraction ($f_{clay}$) by the formula (Brisson and Perrier, 1991):

$$SM_{min} = 0.15 f_{clay} \quad (5)$$

and the maximum SM value is set to the SM at saturation, which can be estimated from sand fraction ($f_{sand}$) as in Cosby et al. (1984).

$$SM_{max} = 0.489 - 0.126 \times f_{sand} \quad (6)$$

## 3.2 New approach: Combined radar/thermal data

SMP of Equation (3) is estimated using a piecewise linear relationship between $SMP_{Ts}$ and $\sigma^0_{pp}$:

$$SMP_{\sigma+Ts} = \begin{cases} 1, & \text{if } SMP_{Ts} \geq 1 \\ a\,\sigma^0_{pp} + b\,, & \text{if } 0 < SMP_{Ts} < 1 \\ 0, & \text{if } SMP_{Ts} \leq 0 \end{cases} \quad (7)$$

with *a* and *b* being two empirical parameters and $SMP_{Ts}$ defined as:

$$SMP_{Ts} = \frac{T_{s,dry} - T_s}{T_{s,dry} - T_{s,wet}} \quad (8)$$

with $T_s$ being the observed soil temperature and $T_{s,wet}$ and $T_{s,dry}$ the soil temperature in fully wet and dry conditions, respectively. Both *a* and *b* parameters were calibrated using L7/L8 thermal data by comparing $SMP_{\sigma+Ts}$ to $SMP_{TS}$. In this paper, $T_s$ was derived from either *in situ* Apogee or satellite L7/8 thermal data. Both temperature endmembers were simulated by running a soil energy balance (EB) model forced by meteorological data and with a prescribed soil resistance to evaporation $r_{ss}$ (Merlin et al., 2016; Stefan et al., 2015). In addition, a sensitivity analyses was performed using the contextual method to assess the impact of uncertainties in temperature endmembers on SM estimation. Equations of EB model are provided in Appendix A. In practice, $r_{ss}$ was set to 0 and ∞ for $T_{s,wet}$ and $T_{s,dry}$ respectively.

We considered that $SMP_{Ts}$ is a good approximation of the soil evaporative efficiency (SEE) defined as:

$$SEE = \frac{LE_s}{LE_p} \quad (9)$$

with $LE_s$ and $LE_p$ being the actual and potential soil evaporation, respectively. SEE is known to be strongly dependent on SM (e.g. Nishida et al., 2003) and its expression as a function of soil temperature (namely $SMP_{Ts}$ in Equation 9) has been found to be valid in a large range of conditions (Merlin et al., 2016). This allows for simply relating $SMP_{Ts}$ to SM using the piecewise linear SEE model (Budyko, 1956; Manabe, 1969):

$$SEE = \frac{SM}{SM_c} \quad (10)$$

with the $SM_C$ being equal to ¾ of the soil moisture at field capacity $SM_{fc}$ ($m^3\ m^{-3}$). At this SM value, the SEE reaches its maximum, at which the evaporation process switches from moisture-limited to energy-limited conditions. $SM_{fc}$ is estimated as in Mahfouf and Noilhan, (1996) by the formula:

$$SM_{fc} = 0.089 \times (f_{clay})^{0.3496} \quad (11)$$

Calibration of a and b parameters of $SMP_{\sigma+Ts}$ (Equation 7) using independent $SMP_{Ts}$ (Equation 8) estimates relies on the condition that $SMP_{Ts}$ does not reach its saturation value (1), meaning that SM does not exceed $SM_C$. A direct consequence is that the SM endmembers in Equation (3) are set to $SM_{res}$ and $SM_C$ for $SM_{min}$ and $SM_{max}$, respectively. Unlike $SMP_{Ts}$, the radar signal does not reach a maximum threshold except for very moist soils (Bruckler et al., 1988; Chanzy, 1993; Dobson and Ulaby, 1981). Therefore, the SM retrieved from the combined thermal and radar data is calibrated for SM values between $SM_{res}$ and $SM_C$ (corresponding to $SMP_{Ts} < 1$), but it may exceed the $SM_C$ value for backscatter values larger than $\frac{SM_C - b}{a}$.

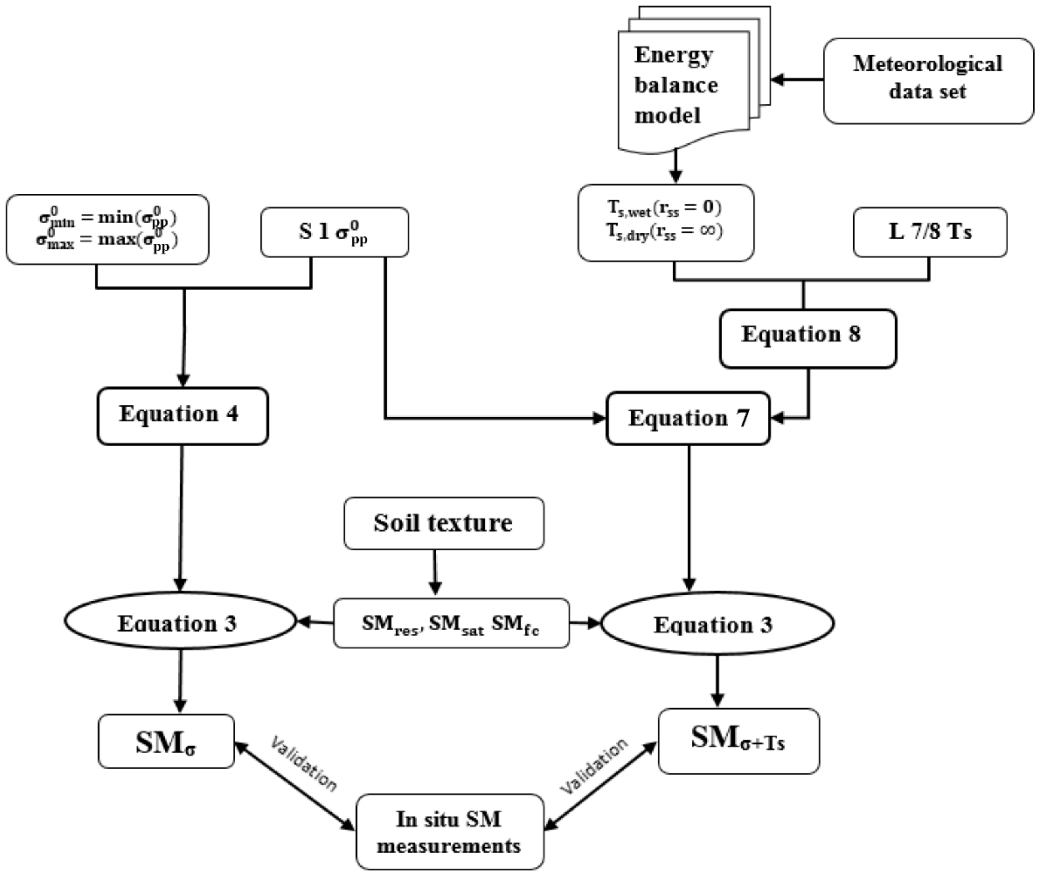


*Figure 3: Flowchart for the benchmark (radar only, on the left) and new (combined thermal and radar, on the right) SM retrieval approaches.*

To assess the $SMP_{Ts}$ (SM) relationship, Figure 4 plots the $SMP_{Ts}$ simulated by Equation (8) as a function of SM for *in situ* (at Landsat overpass time) and L7/8 data, separately. Although $SMP_{Ts}$ generally ranges

from 0 to 1, some negative values were observed in the lower SM range. This is due to the fact that $T_{s,dry}$ and $T_{s,wet}$ were estimated by the EB model, independently from $T_s$ measurements. A nonlinear behaviour of $SMP_{Ts}$ was obtained when considering the full SM range. The piecewise linear SEE model was superimposed for the values of SM ranging from 0 to $SM_C$ and for SM values larger than $SM_C$. $SMP_{Ts}$ value were consistent with the simple SEE model of Budyko, (1956) and Manabe (1969), for both *in situ* and satellite thermal data sets. However, note that most of the $SMP_{Ts}$ values derived from Landsat data (blue colour) correspond to the driest period. This is due to both the relatively low temporal resolution of thermal data and also to the cloud coverage on several wet overpass dates. Nonetheless, Landsat-derived $SMP_{Ts}$ estimates were strongly consistent with *in situ*-derived $SMP_{Ts}$ estimates and still range between 0 and 1.

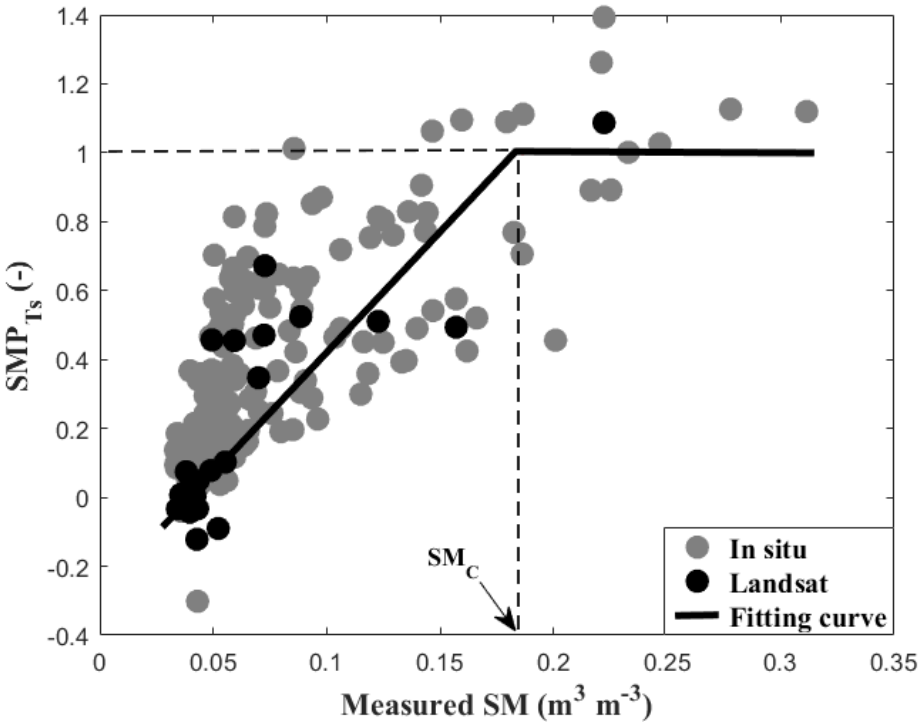


*Figure 4: The $SMP_{Ts}$ derived from 1) in situ data collected at 11:00 am and 2) L7/L8-derived data is plotted as a function of in situ SM at Sidi Rahal site.*

# 4. Results and discussions

## 4.1 Sensitivity of VV- and VH-polarized data to soil moisture

The comparison between VV and VH polarization was undertaken over the Sidi Rahal site where the longest time series of S1 data was available. As shown in Figure 5, the VV polarization is significantly correlated with SM, whereas the VH polarization is poorly correlated ($R^2$=0.47 and 0.28, respectively). Previous studies have shown the same results (Eweys et al., 2017; Gherboudj et al., 2011), and our findings

were consistent with the work of Baghdadi et al. (2006b), where they use a large database over ten years to study the sensitivity of the radar signal to SM over bare soils. VH polarization was found to be sensitive to roughness and to the vegetation volume, due to the depolarization effect by vegetation-volume-scattering, which mainly depends on the vegetation characteristics (Chauhan and Srivastava, 2016; Gao et al., 2017; Karjalainen et al., 2014). The change in polarization between the radar pulse and the echo (depolarization phenomena) is related to the physical structure of the scattering surface (rough surface). In contrast, SM is linked to dielectric soil constant using the dielectric mixing model (Dobson et al., 1985).

The sensitivity of the radar backscatter to SM is estimated as 0.30 and 0.14 $dB/m^3$ $m^{-3}$ for VV and VH polarization, respectively. The same sensitivity of the VV-polarized data to SM was observed in Le Hégarat et al. (2002), Quesney et al. (2000) and Srivastava et al. (2003). The dispersion and the curvilinear shape of measurements points may be attributed to roughness effects (Holah et al., 2005; Le Morvan et al., 2008).

Incorporating the roughness effect is proven to be necessary when monitoring large areas with different conditions (different soil texture and roughness). Different studies are thus attempted to incorporate the effect of surface roughness in the SM retrieval algorithm. Using data collected along multi-incidence angles requires a simultaneous availability of SAR data at lower and higher incidence angles (Srivastava, 2007). To overcome the (mostly general) unavailability of data at multi-incidence angles, several studies (Srivastava et al., 2008; Ulaby et al., 1986) have used multi-polarized SAR data. Both retrieval methodologies require ground truth measurements of soil moisture and/ or surface roughness for calibration. Contrariwise, the methodology developed in this paper relies on satellite data available world-wide, and does not require ground measurements for calibration. Future studies could make use of both thermal and multi-polarized radar data as additional constraints on the roughness effects on radar-based SM retrievals.

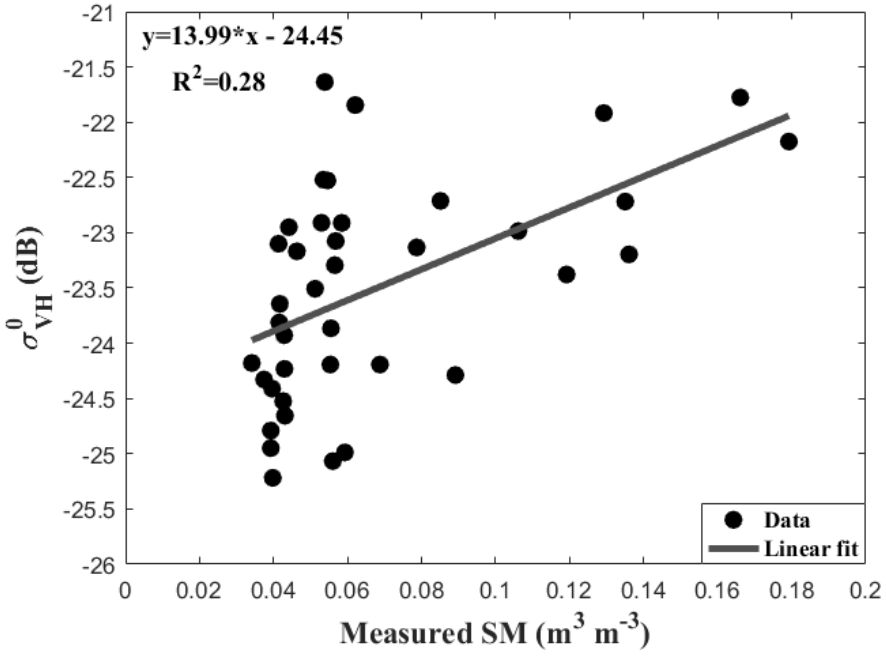


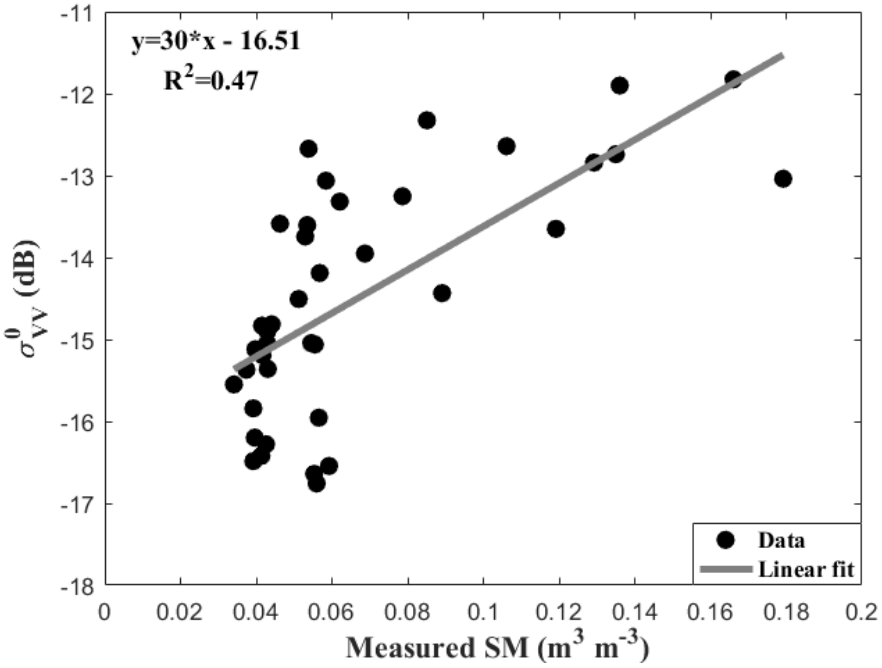


*Figure 5: Radar signal sensitivity to SM for VH (top) and VV (bottom) polarization over the Sidi Rahal site.*

The observation configuration has also an influence on the sensitivity of radar signal to SM, and hence on our capability to retrieve SM from radar data. Several studies showed that the low to medium incidence angles (20°-37°) are the most suitable for SM retrieval using C-band data (Holah et al., 2005; Le Hégarat et al., 2002; Quesney et al., 2000; Srivastava et al., 2003; Zribi et al., 2008). Baghdadi et al. (2008) and Holah et al. (2005) found that the radar sensitivity decreases with increasing incidence angle. Moreover, the azimuthal angle changes with the ascending or descending passes. However, in our case, the study site

is flat and the incidence angle is relatively constant (40°) so we observed no significant difference in terms of SM sensitivity between the data collected on ascending and descending overpasses. Hence, the sensitivity of radar data to the azimuthal angle seemed to be negligible in this study.

As a best option among the two different available polarizations to retrieve top SM, the VV polarization is used throughout the rest of the manuscript.

## 4.2 Relationship between thermal-derived $SMP_{Ts}$ and radar signal

Figure 6 plots $SMP_{Ts}$ against S1 $\sigma^0_{vv}$ for the L7/8 thermal data over the Sidi Rahal and the R3 study site, separately. For the full range of $SMP_{Ts}$ [0-1], we observed a nonlinear behaviour between the Landsat-$SMP_{Ts}$ and the $\sigma^0_{vv}$. So as an attempt to approach linearly $SMP_{Ts}$ ($\sigma^0_{vv}$) and in order to define the calibration coefficient of the piecewise linear model defined in Equation 7, the $SMP_{Ts}$ full range is split into 2 distinct classes separated by the mid-value (0.5). The $SMP_{Ts}$ and $\sigma^0_{vv}$ values falling into each class (< and > to 0.5) provide a centroid point per class. The crossing over between the linear segment passing through the two centroid points and the line SMP = 0 and SMP = 1 allows to define the calibration parameters over each study site separately. From a physical point of view, the 0.5 was taking as a mid-value at which the evaporation process switches from mostly moisture-limited to mostly energy-limited conditions (Merlin et al., 2016). Results of the calibration using Landsat data lead to values of 0.25 $dB^{-1}$ and 3.89 (unitless) for *a* and *b* over Sidi Rahal site and (0.26 $dB^{-1}$ and 4.16 for R3 sites), respectively.

In order to detect the impact of the median value to the calibration parameters (*a* and *b*), and to the retrieved SM, we performed a sensitivity analysis for different mid-values [0.40, 0.45, 0.50, 0.55, and 0.60]. Results are presented in Table 3.

*Table 3: Sensitivity analysis of the calibration results to the mid-value.*

| | **Sidi Rahal** | | | | | **R3** | | | | |
|---|---|---|---|---|---|---|---|---|---|---|
| **Mid-value** | **Calibration parameters a / b** | **SM ($m^3$ $m^{-3}$)** | | | | **Calibration parameters a / b** | **SM ($m^3$ $m^{-3}$)** | | | |
| | | **$R^2$** | **RMSE** | **MBE** | **Slope/intercept** | | **$R^2$** | **RMSE** | **MBE** | **Slope/intercept** |
| **0.40** | **0.20 / 3.25** | 0.64 | 0.03 | 0.01 | 1.00/0.01 | **0.25 / 4.03** | 0.59 | 0.04 | 0.01 | 1.01/0.01 |
| **0.45** | **0.20 / 3.25** | 0.64 | 0.03 | 0.01 | 1.00/0.01 | **0.25 / 4.03** | 0.59 | 0.04 | 0.01 | 1.01/0.01 |
| **0.50** | **0.25/ 3.89** | 0.62 | 0.03 | 0.01 | 1.06/0.01 | **0.26 / 4.16** | 0.59 | 0.04 | 0.0 | 1.03 / -0.0 |
| **0.55** | **0.48 / 7.44** | 0.51 | 0.06 | 0.02 | 1.37/0.00 | **0.25 / 4.13** | 0.59 | 0.04 | 0.01 | 1.02/0.00 |
| **0.60** | **0.48 / 7.44** | 0.51 | 0.06 | 0.02 | 1.37/0.00 | **0.25 / 4.03** | 0.58 | 0.04 | 0.01 | 0.99 /0.01 |

To help interpret these results shown in Table 3, a standard deviation (SD) has been calculated between the values of the *a* parameter for the different mid-values for each site separately. We found that SD is much

larger for Sidi Rahal (0.14) than for R3 (0.004) sites due to the lack of wet conditions encountered in the SEE time series at Sidi Rahal site. As it seen in Table 3, the sensitivity analysis shows that the method is not sensitive to the median value for the R3 sites, where the parameters slightly vary from one to another case, thus reveals very stable results in terms of SM retrievals. In contrast, the influence of the median value appears significantly over the Sidi Rahal site, which affects a lot the SM estimates. Such a sensitivity analysis indicates that the mid-value should be set appropriately, by keeping a sufficient number data points in each of both SEE classes, especially for time series containing mainly dry or mainly wet conditions.

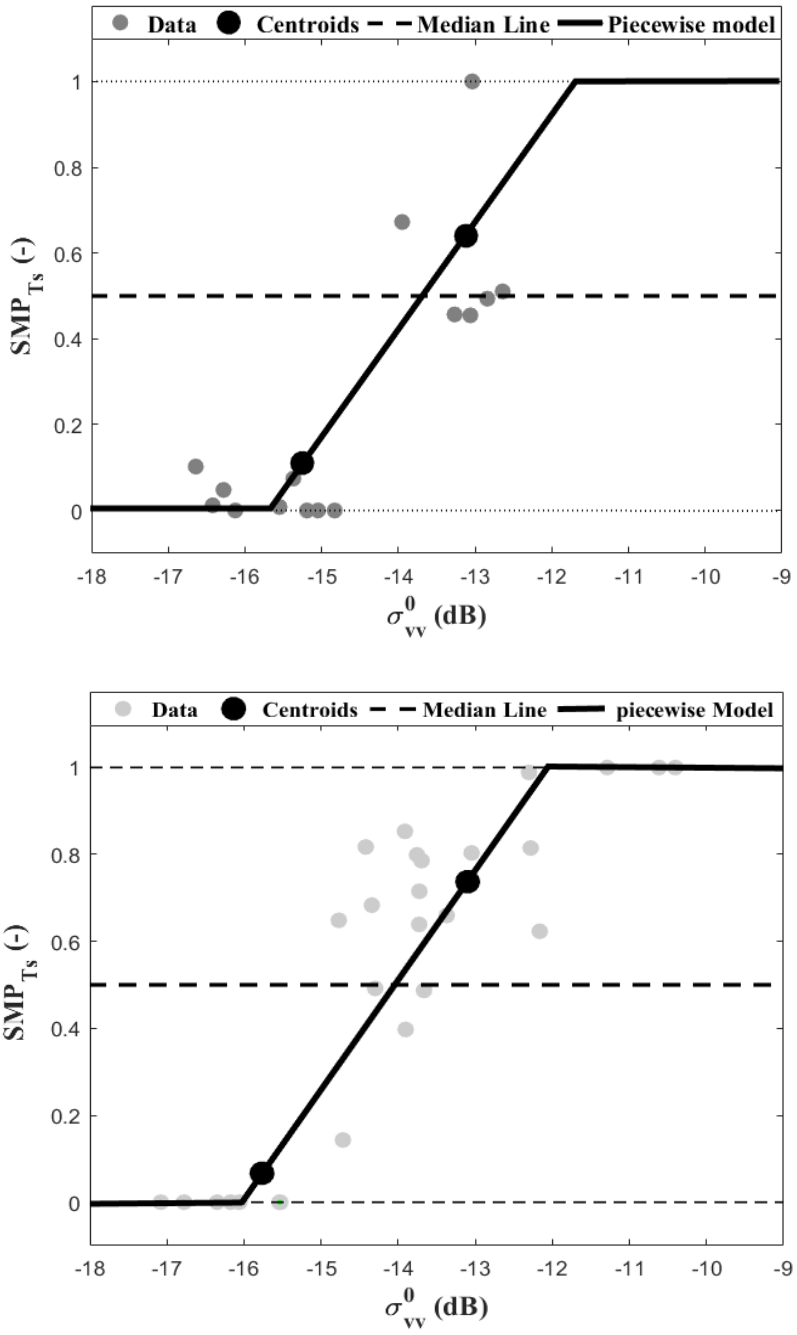


*Figure 6: $SMP_{Ts} - \sigma^0_{vv}$ relationship using $T_s$ derived from Landsat data over Sidi Rahal (top plot) and R3 (bottom plot) site. The solid line represents the assumed piecewise linear model.*

## 4.3 SM retrievals

The classical and new approaches were tested and examined by comparing the retrieved SM with *in situ* measurements. The calibration and validation of the new approach was performed separately at each site (on a pixel basis), having two different soil textures: Sidi Rahal site has a sandy soil while the two other sites in the R3 perimeter are characterised by a clayey soil. Figure 7 compares SM retrievals with *in situ* measurements for the benchmark and new approach for the studied sites, and a validation of the new approach using *in situ* $T_s$ has been also presented over Sidi Rahal site when *in situ* $T_s$ data are available. Results of this comparison, in terms of determination coefficient ($R^2$), slope and intercept of the linear regression, mean bias error (MBE) and root mean square error (RMSE) are presented in Table 4.

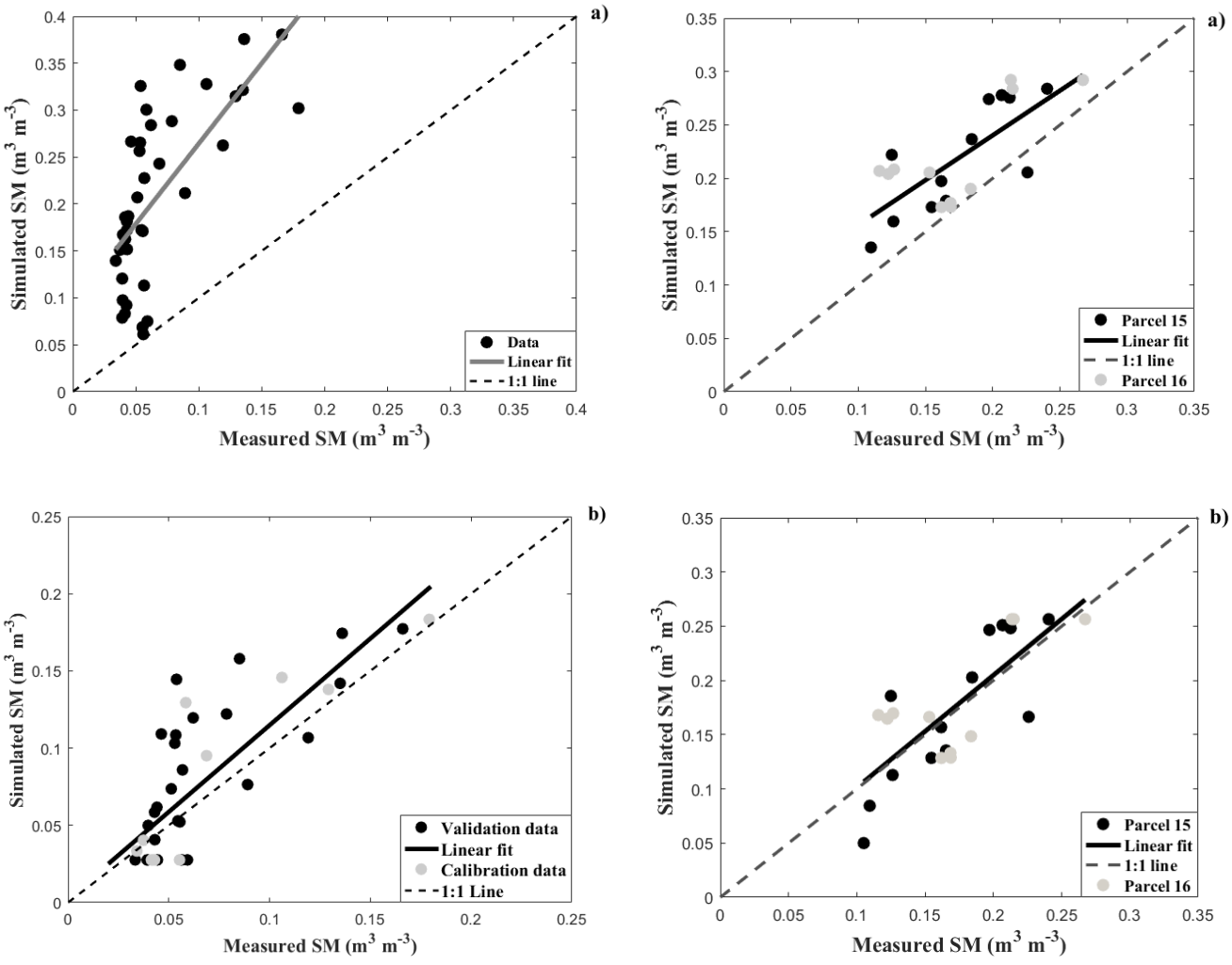

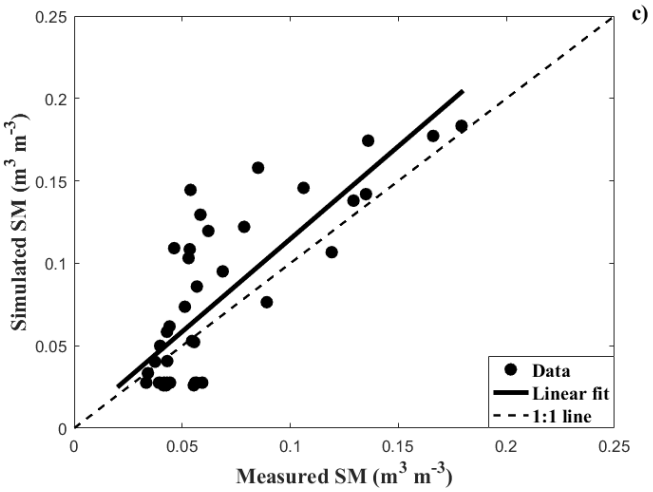


*Figure 7: Estimated versus measured SM using the benchmark approach (a), new approach (b) and in situ validation (c) over Sidi Rahal (left plots) and R3 (right plots) site.*

*Table 4: $R^2$, RMSE, MBE (simulated – observed), and the slope/intercept for the linear regression between simulated and observed SM for the classical and the new approach for Sidi Rahal and R3 sites.*

| Sites | Approach | | $R^2$ | RMSE ($m^3\ m^{-3}$) | MBE ($m^3\ m^{-3}$) | Slope/intercept (-) / ($m^3\ m^{-3}$) |
|---|---|---|---|---|---|---|
| **Sidi Rahal** | **Classic** | | 0.47 | 0.16 | 0.14 | 1.71 / 0.09 |
| | **New** | **all dates** | 0.64 | 0.03 | 0.01 | 1.12 / 0.002 |
| | | **dates when L7/8 & S1 data available (not shown here)** | 0.79 | 0.03 | 0.00 | 1.2 / -0.007 |
| | | ***In situ* validation** | 0.64 | 0.03 | 0.01 | 1.12 / 0.002 |
| **R3** | **Classic** | | 0.56 | 0.05 | 0.04 | 0.84 / 0.07 |
| | **New** | | 0.59 | 0.04 | 0.00 | 1.03 / -0.002 |

The benchmark method shows a systematic overestimation, and a kind of curvilinear relationship especially in the Sidi Rahal site whereas the new methodology offers a good consistency with ground-truth measurements. The linear scaling between $\sigma^0_{vv}$ and SM can explains the overestimation observed using the classical approach, since the two coefficients of the linear relationship are derived from extreme values of SM and $\sigma^0_{vv}$. Note that this effect is all the more visible as extreme (wet) SM values have not been reached at the time of S1 overpasses, despite the high temporal resolution of S1 and the relatively long time period. We argue that the main advantage of the proposed method is to provide robust reference points for calibrating the $\sigma^0_{vv}$ (SM) relationship, even for time series that do not contain extreme SM conditions. In addition, the calibration of the Equation (7) allows for taking into account possible nonlinear behaviours of the $\sigma^0_{vv}$ (SM) relationship, especially in dry to very dry conditions. The radar signal can be only calibrated

using thermal data when both satellites are concurrent or are quasi concurrent. It is reminded that over the study area both $T_s$ and backscatter coefficients were available at approximately (one day difference) the same time. A sensitivity analysis was undertaken to assess the impact of a systematic error in LST on SM retrieval results. Based in the finding (results not shown), an error in LST estimations (±3 °C) would have a relatively small effect (maximum additional error of 0.02 $m^3$ $m^{-3}$) in the SM estimations. Note that a bias in Landsat LST would have no effect on SM retrievals in the case of using contextual methods, instead of using an energy balance model to determine $T_{s,dry}$ and $T_{s,wet}$. When L7/8 and the S1 data were available in Sidi Rahal site, the results reveal a high $R^2$ of 0.79 with an RMSE of 0.03 $m^3$ $m^{-3}$ which decrease the bias. As seen in Table 4, the radar/thermal combining approach provides a slightly higher $R^2$ value and a lower RMSE compared to the classical (radar only) approach. This improvement result is in an almost negligible mean difference between the estimated and *in situ* SM. The statistical outputs parameters confirm that the new approach estimates SM accurately, regardless of the soil composition. Results in terms of SM accuracy indicate that the loss of spatial resolution (from the aggregation of radar data from 20 m resolution to crop field scale) has a lower impact than the roughness effects that need to be taken into account at the crop field scale. A slope correction is observed (close to 1) using the new approach with an almost null intercept using satellite data whereas the conventional approach provides a higher value of both slope and intercept. Note that the one-day difference between Sentinel-1 radar and Landsat LST data, which may be representative of different SM levels (difference estimated as 0.02 $m^3$ $m^{-3}$ over the experimental site), explains part of the uncertainty (estimated as 0.03 $m^3$ $m^{-3}$) in the retrieved SM. We can explain the previous statement by the non-appropriate estimation of $\sigma^0_{vv,min}$ and $\sigma^0_{vv,max}$ for the classical approach, which is based on two assumptions: 1) minimum and maximum SM values are observed at the time of S1 overpasses and 2) the relationship between backscatter coefficient and SM is linear. Note that such a relationship tends to be non-linear (Zribi et al., 2011), with a saturation appearing in the radar signal in the higher range of SM values (Bruckler et al., 1988).

In Figure 7 (Sidi Rahal site), a significant phenomenon was observed for the low SM values, which correspond to low backscatter values. In this range, *in situ* SM do not change with radar backscatter. This observed phenomena can be explained by the deeper penetration of the radar when the soil surface gets drier. In addition, the radar signal tends to be more sensitive to roughness variations in very dry conditions (Boisvert et al., 1997). We did not observe this effect over R3 sites because of the wetter conditions encountered over the irrigated perimeter. In addition, the SM in the top 5 cm may differ between the two sites, depending on the soil water retention properties and infiltration rates, resulting in variations in the S1 signal (Aubert et al., 2011).

## 4.4 Sensitivity to temperature endmembers

In this study, SEE was derived from the temperature endmembers simulated by an EB model. Therefore, meteorological forcing data are needed as input to the calibration scheme of the radar-based SM retrieval approach. The point is that meteorological data may not be available everywhere with sufficient accuracy. For this reason, remote sensing-based temperature endmembers could be used to fill the gap. In particular, the contextual method has been successfully used to monitor evapotranspiration over large areas, by relying mainly on the distance between the observed LST and the hypothetical LST values in fully dry and wet conditions. Especially, the image-based nature of the contextual method makes it easily applicable to different areas (i.e. the method is self-calibrated). The contextual information contained in remotely sensed LST and vegetation index (such as NDVI) can be extracted by interpreting the LST-NDVI feature space (in the shape of a triangle or trapezoid). This method was firstly proposed by Goward et al. (1985) and has been widely used to monitor soil water content (Kim and Hogue, 2012; Merlin et al., 2008; Sandholt et al., 2002; Sobrino et al., 2012), evaporative fraction (Batra et al., 2006; Wang et al., 2006), evapotranspiration (Merlin, 2013; Stefan et al., 2015), drought (Wan et al., 2004), surface resistance (Nemani and Running, 1989), land use and land cover change (Julien and Sobrino, 2009). There are various popular models based on the contextual method such as: surface energy balance algorithm for land (SEBAL) (Bastiaanssen et al., 1998), mapping evapotranspiration at high resolution with internalized calibration (METRIC) (Allen et al., 2007) and simplified surface energy balance index (S-SEBI) (Roerink et al., 2000).

In this study, the contextual method is used to derive the soil temperature endmembers over a 8 by 8 $km^2$ area covering the experimental sites. Once the polygon identified, the $T_{s,dry}$ and $T_{s,wet}$ correspond to fully dry and wet conditions over bare soil, which are characterised by the largest and smallest LST in the lower NDVI range (< 0.2), respectively. A visual representation of the LST-NDVI polygon and the dry and wet conditions over bare soil is proposed in Figure 8.

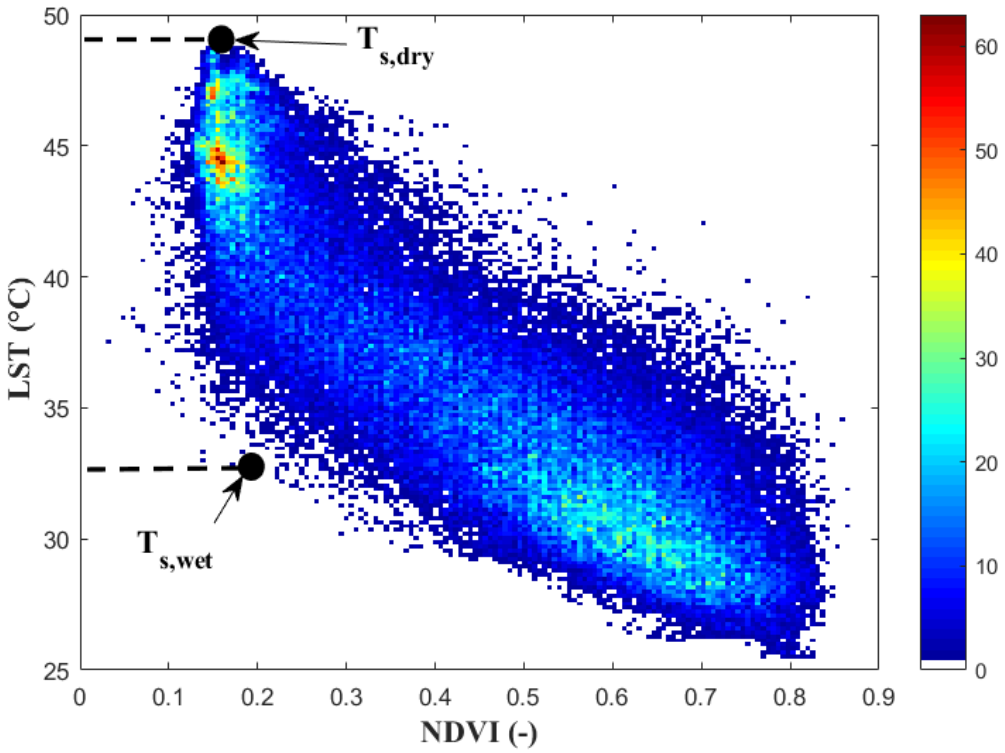


*Figure 8: Density scatter plot of the relationship between LST and NDVI for all (30m × 30m) cells in R3 area. The black dots represent the fully dry and wet condition over bare soil.*

As a first assessment of the performance of the space-based approach, the $T_{s,dry}$ and $T_{s,wet}$ estimated by the contextual method using Landsat data are compared against the ones modelled by EB model. The analysis is performed at the Landsat overpass time over the Sidi Rahal and R3 areas separately. Figure 9 plots the T endmembers derived from EB model versus the space-based ones for the studied areas separately. A comparison between air temperature ($T_{air}$) and the $T_{s,wet}$ simulated by EB model is also presented. The statistical results in terms of $R^2$ and RMSE are shown in Figure 9.

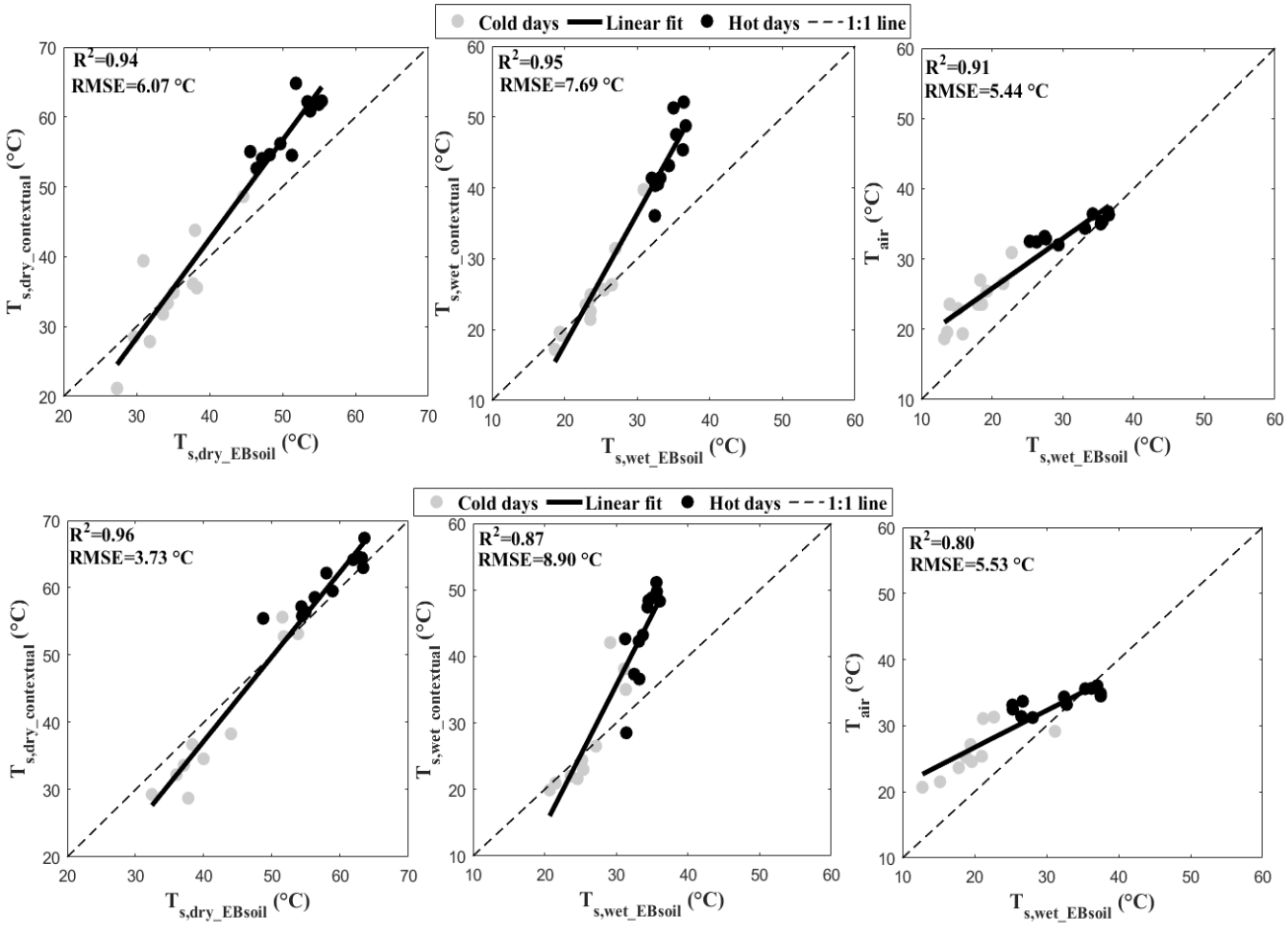


476

477

478 *Figure 9: EB-simulated versus space-based soil temperature endmembers ($T_{s,wet}$ and $T_{s,dry}$) for R3 (top plots) and*
479 *Sidi rahal (bottom plots) sites separatly.*

480 A strong consistency is noticed between EB-derived and image-based extreme temperatures, especially for
481 $T_{s,dry}$. Statistical results in terms of $R^2$ and RMSE between modelled and remotely-sensed $T_s$ endmembers
482 indicate similar results for both sites. Results tend to be more evenly scattered along the regression line.
483 However, the image-derived $T_{s,wet}$ clearly overestimates EB-simulated $T_{s,wet}$ in the higher range (hot days).
484 Such an overestimation especially occurs in summer (June 01$^{st}$ to September 25$^{th}$, 2016) when wet
485 conditions are poorly represented.
486 The idea behind using the contextual method to derive temperature endmembers is to analyse the sensitivity
487 of the SM estimation to uncertainties in $T_{s,dry}$ and $T_{s,wet}$ estimates. The extreme $T_s$ are used as an input in
488 Equation 8 in order to assess the potential of the contextual method against the EB method. The retrieved
489 SM using the $T_s$ endmembers extracted from LST-NDVI polygons is evaluated against *in situ*
490 measurements over the study areas. At Sidi Rahal, the use of image-based $T_s$ endmembers leads to small
491 values of $SMP_{Ts}$ (< 0.3), which makes our approach inapplicable in this case as wet reference points are
492 lacking to build the calibration equation. This is due to the overestimation of $T_{s,wet}$ by the contextual method.
493 In addition, the Sidi Rahal (8 × 8 km$^2$) area experienced the highest observed temperature (very close to

$T_{s,dry}$) leading to a small SEE values. The contextual method was also tested over the R3 area. In order to investigate the influence of $T_{s,wet}$ estimation, the new approach is also tested by using $T_{air}$ instead of $T_{s,wet}$ (in addition to contextual $T_{s,dry}$).

Figure 10 shows the estimated SM using the image-based $T_s$ endmembers against ground measurements acquired from the R3 study site. The statistical values such as the slope of the linear regression, $R^2$, RMSE and MBE between retrieved and *in situ* SM are reported in Table 5.

*Table 5: $R^2$, RMSE, MBE and slope/intercept of the linear regression between retrieved and observed SM for the classical and the new approach for R3 sites using contextual $T_s$ endmembers.*

| **Temperature endmembers** | | **$R^2$ (-)** | **RMSE ($m^3$ $m^{-3}$)** | **MBE ($m^3$ $m^{-3}$)** | **Slope / intercept (-) / ($m^3$ $m^{-3}$)** |
|---|---|---|---|---|---|
| **Classic** | | 0.56 | 0.05 | 0.04 | 0.84 / 0.07 |
| **New** | **Contextual $T_{s,wet}$ and $T_{s,dry}$** | 0.56 | 0.04 | 0.03 | 0.52 / 0.11 |
| | **$T_{air}$ and contextual $T_{s,dry}$** | 0.50 | 0.04 | 0.01 | 0.99 / 0.01 |

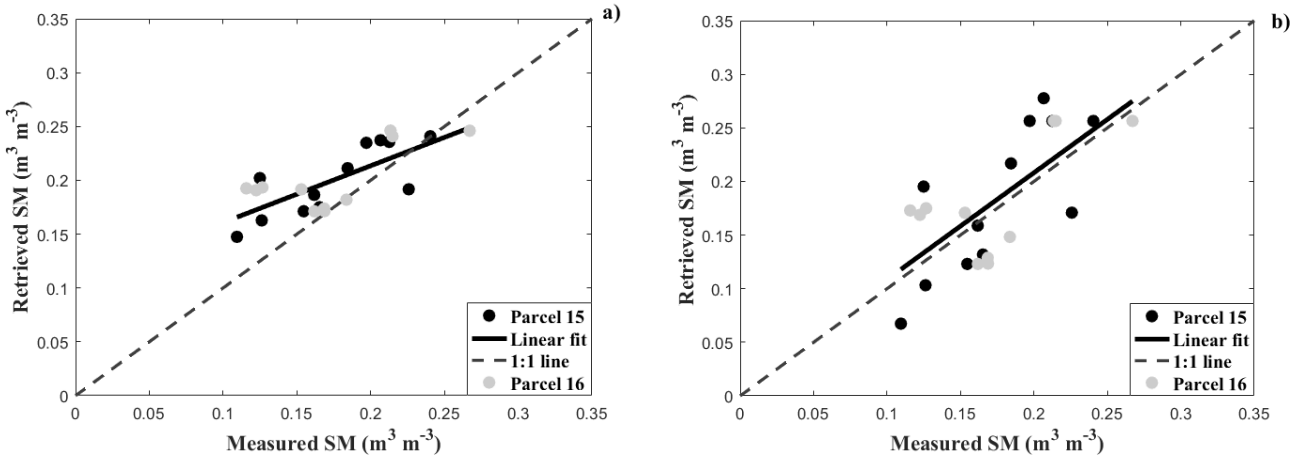


*Figure 10: Retrieved versus measured SM using the new approach over R3 sites using: a) contextual $T_s$ endmembers and b) contextual $T_{s,dry}$ and $T_{air}$ instead of $T_{s,wet}$.*

After using the $T_s$ endmembers extracted from contextual information, the new method shows an improvement in terms of RMSE (0.04 $m^3$ $m^{-3}$ compared to 0.05 $m^3$ $m^{-3}$ for the classical approach). In contrast, the classical approach offers a better slope (close to 1) compared to the new approach (Figure 10 a). The poor slope obtained using the new approach is probably due to the overestimation of $T_{s,wet}$ by using the contextual method especially during summer, when wet conditions were not met over the study area. To discriminate the effect of image-based $T_{s,wet}$ on SM estimation, $T_{air}$ was used as a better proxy of $T_{s,wet}$ at the satellite overpass time. Results (Figure 10 b) listed in table 6, revealed a slightly poorer $R^2$ (0.50) in contrast with the classical approach (0.56), except that the new approach offers a slope equal to 1 with a null intercept in addition to smaller bias (0.01 versus 0.04 $m^3$ $m^{-3}$) compared to the classical approach. As a

brief summary of this sensitivity analysis, it is found that EB temperature endmembers are generally more robust than image-based temperature endmembers. Nevertheless, in certain conditions (e.g. semi-arid irrigated areas containing quasi continuously wet and dry conditions), the contextual method could offer an efficient alternative to calibrate the radar-based SM retrieval approach, especially in the regions where meteorological data are not available with sufficient accuracy.

An additional sensitivity analysis was performed in order to assess the impact of the surface roughness on radar and LST data, as well as on the energy balance model (represented by $Z_{0h}$ and $Z_{0m}$ the roughness length for heat and momentum) on the modelled extreme temperatures and the retrieved SM (via simulated $T_{s,dry}$ and $T_{s,wet}$). It is found (results not shown) that the modelled LST remains rather stable when changing the roughness parameters by 1 order of magnitude. Note that the stability of LST with respect to soil roughness is fully consistent with all contextual methods that rely on this assumption as well (ex. by setting the maximum observed LST to $T_{s,dry}$ ).

## 4.5 Soil evaporation estimation

The tight coupling between soil evaporation and SM in semi-arid areas is used to calibrate the radar-SM relationship using thermal-derived SEE estimates. As a step further in the assessment of the proposed methodology, the soil evaporation was estimated from either the radar-based SM, the thermal-derived SEE, or the thermal-calibrated radar-based SM. Note that soil evaporation represents an important component of the water budget over semi-arid regions. Although various evaporation formulations exist as a function of SM (Chanzy, 1991; Chanzy and Bruckler, 1993; Mahfouf J.-F. and Noilhan, 1991), the uncertainty in evaporation models remains relatively large especially when applied to a range of surface conditions (Merlin et al., 2016). Even though remote sensing data have strong potential for better constraining the evaporation process (Chanzy and Bruckler, 1993; Merlin et al., 2017), the characterisation of model parameters using available remotely sensed land surface temperature and SM observations is still not well identified.

As a complementary assessment of the synergy between radar- and thermal-based techniques for SM retrieval, both approaches were thus inter-compared in terms of soil evaporation estimates over the Sidi Rahal site, when eddy covariance measurements are available. In this sub-section, $LE_s$ was estimated using Equation 9, and the potential evaporation estimated using the same energy balance model (described in the Appendix) as that used to estimate temperature endmembers. The SEE used as input to Equation 9 was derived either from L7/8 Thermal data (Equation 8) or S1 backscatter (Equation 4).

Regarding the SM-based SEE model, two different parameterizations are suggested by setting the parameter to $SM_C$ (Equation 10) or $SM_{sat}$:

546 $$SEE = \frac{SM_{\sigma+Ts}}{SM_{sat}} \quad (12)$$

547 with $SM_{\sigma+Ts}$ ($m^3\ m^{-3}$) being the SM estimated using the synergistic approach between Landsat and S1 data.
548 Figure 11 and Table 6 presents the results of the soil evaporation estimation using the above four models.

549 *Table 6: Error statistics between simulated and observed evaporation over Sidi Rahal site.*

| **Input data** | | **$R^2$** | **RMSE (W $m^{-2}$)** | **MBE (W $m^{-2}$)** |
|---|---|---|---|---|
| **Thermal data only** | | 0.36 | 64.2 | -14.5 |
| **Radar data only** | | 0.41 | 166 | 130 |
| **Combined radar and thermal data** | **Equation (10)** | 0.63 | 103 | 77 |
| | **Equation (12)** | 0.63 | 26.5 | -0.14 |

550

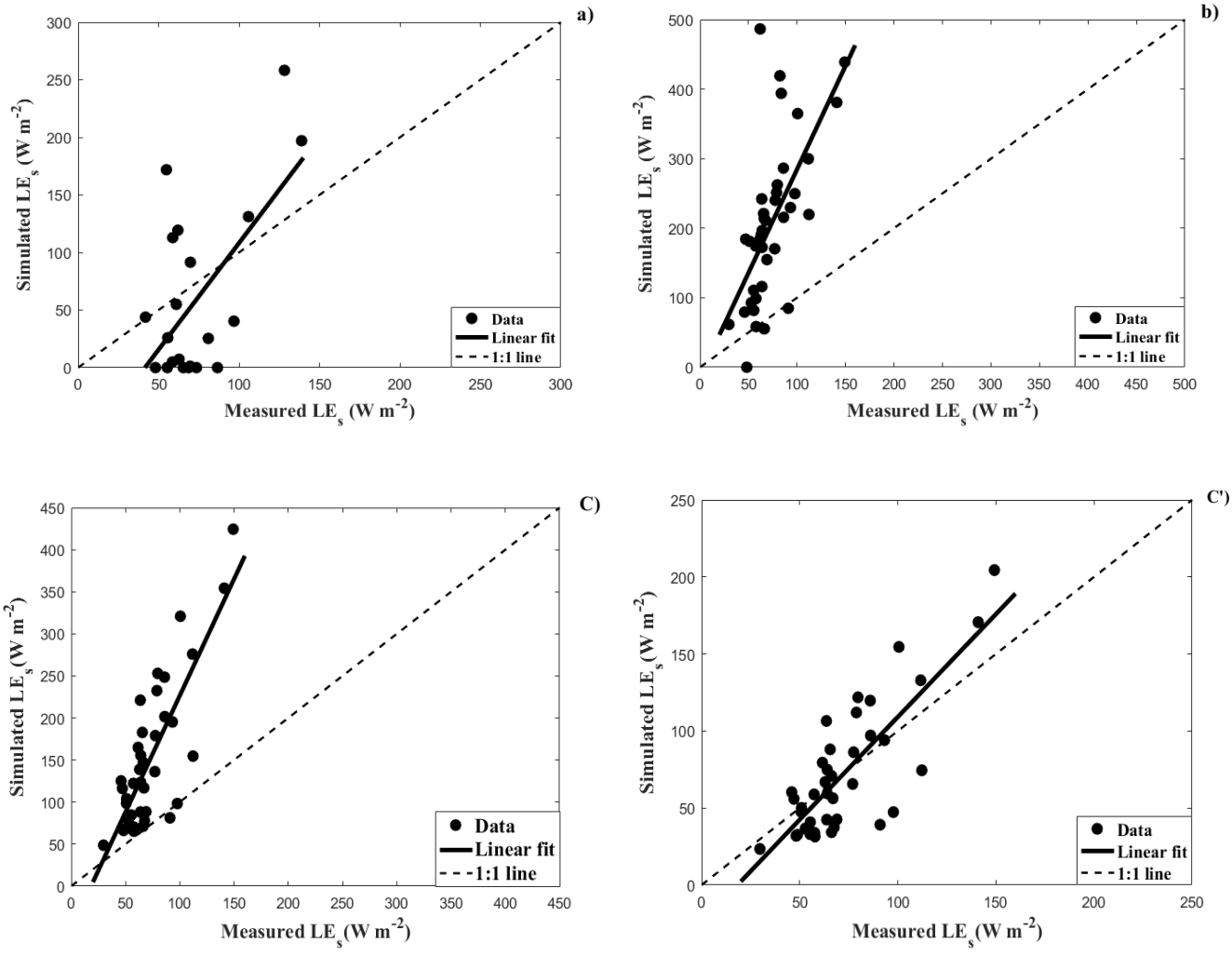


551

552 *Figure 11: Comparison at the Sidi Rahal site between simulated and observed soil evaporation for an SEE model*
553 *driven by a) LST data, b) radar data, and combined radar and Landsat data using c) $SM_C$ and c') $SM_{sat}$ parameter.*

554 Table 7 shows that the combination between radar and thermal data (Figure 11 c and c') provides better
555 evaporation results than using each satellite separately (Figure 11 a and b). The evaporation estimates

derived from thermal data only are greatly uncertain. This could be due to the loss of sensitivity of land surface temperature to the 0-5 cm SM in very hot and dry conditions. The use of radar data only provides a much better correlation between simulated and observed soil evaporation, but estimates values are systematically larger than those observed by eddy covariance. This effect is also visible with the thermal/radar combined approach with $SM_C$ parameter. When setting the SM-based SEE parameter to $SM_{sat}$, the systematic overestimation disappears with a determination coefficient and bias between simulated and observed evaporation of 0.63 and 0.14 W $m^{-2}$. Better results obtained by changing the SM-based SEE parameter from $SM_C$ to $SM_{sat}$ could be attributed to soil profile heterogeneities, which are very strong in semi-arid regions. In fact, the microwave-derived SM generally corresponds to the first cm of soil whereas the radiometric soil temperature is representative of a soil layer that is much thinner (approximately 1 mm). The discrepancy between the sensing depth of microwave and thermal data partly explains the difference in thermal-based and SM-based SEE models in this case (Merlin et al., 2017) .

# 5. Conclusion

This paper proposes a new approach to retrieve the near-surface (5 cm) soil moisture (SM) over bare soils by combining Sentinel-1 C-band radar and Landsat-7/Landsat-8 thermal data. The methodology is based on the thermal-derived soil evaporation efficiency (SEE) to calibrate the radar backscatter-SM relationship on a (100 m resolution) pixel basis. In practice, the observed relationship between the pp (VV or VH) polarized backscatter coefficient $\sigma^0_{pp}$ and thermal-derived SEE was modelled by a piecewise linear regression model. Calibration of the piecewise model was performed by 1) computing the two centroids of the ($\sigma^0_{pp}$, SEE) points with SEE>0.5 and SEE<=0.5, 2) plotting the line passing through both centroids and 3) estimating the two crossing points of that line with the lines defined by SEE=0 and SEE=1. The retrieval approach was evaluated by comparing the remotely sensed SM to *in situ* measurements at two contrasted soil texture experimental sites (Sidi Rahal has sandy soil while R3 perimeter has clayey soil). The radar/thermal synergistic method was also compared to a classical (based on radar only) method.

When comparing Sentinel-1 VV- and VH-polarized data, we found that the VV backscatter coefficient is more sensitive than the VH backscatter coefficient to the SM variation, even with the relatively high incidence angle (approximately 40°) of Sentinel-1 observations over the studied sites. Consequently, the radar/thermal synergistic SM retrieval approach was tested with the VV-polarized data. The determination coefficient between remotely sensed and *in situ* SM is 0.64 and 0.59 with the new approach, compared to 0.47 and 0.56 for the classical approach over Sidi Rahal and R3 site, respectively. Moreover, the bias between remotely sensed and *in situ* SM is very significantly reduced when including thermal data, from 0.14 to 0.01 $m^3$ $m^{-3}$ and from 0.04 to 0.00 $m^3$ $m^{-3}$ over Sidi Rahal and R3 site, respectively. As step further,

588 the radar-thermal combining approach is also assessed in terms of soil evaporation estimates. A RMSE of
589 26 W $m^{-2}$ was obtained between simulated and observed evaporation, compared to 64 and 166 W $m^{-2}$ when
590 using the thermal data only and the radar data only, respectively. The synergy between radar and thermal
591 data could thus be used to both improve the SM retrieval at high-spatial resolution and foster the spatial
592 representation of the soil energy-water coupled budget.

593 Those results are very encouraging as they open the path for more synergies between (radar and optical)
594 space missions and (SM and water-energy budget) applications. However, the proposed methodology was
595 only assessed over bare soils. Further research must be undertaken to test the applicability of the calibration
596 method to soils partially and/or fully covered by vegetation canopy, notably by integrating the VH data that
597 are more sensitive to vegetation effects than VV data. Another potential limitation (Table 7) is the temporal
598 frequency of thermal observations. The robustness of the calibration approach mainly relies on the
599 availability of thermal data, at the same time as radar acquisitions. Unfortunately, the thermal data available
600 at high-spatial resolution (100 m with Landsat) currently have a maximum temporal resolution of 8 days
601 (Lagouarde et al., 2014). When the scene will be cloudy, the temporal resolution will be necessarily less.
602 Consequently, the applicability of the proposed thermal/radar synergy over cropped fields will require
603 sufficient thermal images during bare soil periods that is from the sowing date until emergence and during
604 the intercropping periods. It will also require significant SM variations associated with irrigation or rainfall
605 events during those periods. Last but not least, the temperature endmembers used to derive the SEE from
606 thermal data are estimated from an energy balance model forced by meteorological forcing data. The point
607 is that meteorological data may not be available everywhere with sufficient accuracy. Thus, alternative
608 solutions could be imagined, such as the derivation of temperature endmembers from contextual methods
609 relying on remote sensing data solely. Contextual methods are especially well adapted over semi-arid
610 irrigated regions where extremely dry and wet conditions are present within the thermal scene (Stefan et
611 al., 2015).

612 *Table 7: Summarize of the advantages and the drawbacks of the methods used in this paper (radar-only, thermal-*
613 *only and combined radar+thermal).*

| **Radar-only** | **Thermal-only** | **Combined thermal/radar** |
|---|---|---|
| **Advantages:**<br>-Directly linked to SM.<br>- Radar data available at high spatio-temporal resolution.<br>**Drawbacks:**<br>- Highly sensitive to surface roughness effects, which often involves calibration using in situ data. | **Advantages:**<br>- Coupled to SM in moisture-limited conditions via the energy balance equation<br>- Less sensitive to surface roughness<br>**Drawbacks:** | **Advantages:**<br>- Relies on radar data available at high spatio-temporal resolution.<br>- Robust reference points for calibrating the $\sigma^0_{vv}$ (SM) relationship.<br>-Taking into account possible nonlinear behaviours of the |

| | | |
|---|---|---|
| - No saturation issues except for very moist soils. | - Weakly linked to SM when the incoming energy is limiting<br>- Unavailable under cloudy conditions and at night<br>- Low temporal resolution of high-spatial-resolution thermal data | $\sigma^0_{vv}$(SM) relationship.<br><br>**Drawbacks:**<br>- Requires simultaneous thermal/radar observations. |

# Acknowledgments

This study was conducted within the International Joint Laboratory-TREMA (http://trema.ucam.ac.ma/), and received funding from the European Commission Horizon 2020 Programme for Research and Innovation (H2020) in the context of the Marie Sklodowska-Curie Research and Innovation Staff Exchange (RISE) action (REC project, grant agreement no: 645642) http://rec.isardsat.com/. The MIXMOD-E project (ANR-13-JS06-0003-01) is also acknowledged. We would like to thank also the Moroccan CNRST (Centre National pour la Recherche Scientifique et Technique) for awarding a PhD scholarship to Abdelhakim Amazirh.

# List of Figures

# Appendix

**Soil energy balance Model**

Surface energy balance model equation based on the partition of available energy on the surface ($R_n$-G) into sensible and latent heat flux (H and LE):

$$R_n - G = LE + H \quad (A.1)$$

with $R_n$ is the surface net radiation is expressed as:

$$R_n = (1 - \alpha)\, R_g + \varepsilon(R_{atm} - \sigma T_s^4) \quad (A.2)$$

with α (-) being the surface albedo (set to 0.15), $R_g$ (W $m^{-2}$) the global radiation, ε (-) is the surface emissivity (set to 0.95), $R_{atm}$ the atmospheric longwave radiation (W $m^{-2}$) and $\sigma$=5.67×$10^{-8}$ the Stephan-Boltzmann constant (W $m^{-2}$ $K^{-4}$). The downward atmospheric radiation at surface level is expressed as:

$$R_{atm} = \varepsilon_a \times \sigma T_{air}^4 \quad (A.3)$$

where $\varepsilon_a$ is the atmospheric emissivity estimated as in (Brutsaert, 1975):

$$\varepsilon_a = 1.24 \times \left(\frac{e_a}{T_{air}}\right)^{\frac{1}{7}} \quad (A.4)$$

with

$$e_a = e_s(T_{air}) \times \frac{rh_a}{100} \quad (A.5)$$

$rh_a$ (%) being the air relative humidity and $e_s$ the saturated water vapour pressure (kPa) given by:

$$e_s = 0.611 \times e^{\left(\frac{17.27 \times T_{air}}{T_{air}+273.3}\right)} \quad (A.6)$$

The ground flux G is estimated as a fraction of net radiation at the surface $R_n$:

$$G = cg.R_n \quad (A.7)$$

with cg being a fractional empirical coefficient set to 0.2.

The sensible heat flux is given by:

$$H = \rho c_p \frac{T_s - T_{air}}{r_{a,h}} \quad (A.8)$$

The latent heat flux is estimated as:

$$LE = \frac{\rho c_p}{\gamma} \frac{e_s - e_a}{r_{a,h} + r_c} \quad (A.9)$$

Finally, for running the energy balance model, we set LST=$T_{air}$ and look for the value of LST that minimizes the following cost function F (LST):

$$F(T_s) = (R_n - G - H - LE)^2 \quad (A.10)$$

# References


Alexakis, D.D., Mexis, F.D.K., Vozinaki, A.E.K., Daliakopoulos, I.N., Tsanis, I.K., 2017. Soil moisture content estimation based on Sentinel-1 and auxiliary earth observation products. A hydrological approach. Sensors (Switzerland). doi:10.3390/s17061455

Allen, R.G., Tasumi, M., Morse, A., Trezza, R., Wright, J.L., Bastiaanssen, W., Kramber, W., Lorite, I.J., C.W., R., 2007. Journal of Irrigation and Drainage Engineering Satellite-Based Energy Balance for Mapping Evapotranspiration with Internalized Calibration ( METRIC )— Applications. JOURNAL OF IRRIGATION AND DRAINAGE ENGINEERING. doi:10.1061/(ASCE)0733-9437(2007)133

Amazirh, A., Er-Raki, S., Chehbouni, A., Rivalland, V., Diarra, A., Khabba, S., Ezzahar, J., Merlin, O., 2017. Modified Penman–Monteith equation for monitoring evapotranspiration of wheat crop: Relationship between the surface resistance and remotely sensed stress index. Biosystems Engineering 164, 68–84. doi:10.1016/j.biosystemseng.2017.09.015

Attema, E.P.W., Ulaby, F.T., 1978. Vegetation modeled as a water cloud. Radio Science. doi:10.1029/RS013i002p00357

Aubert, M., Baghdadi, N., Zribi, M., Douaoui, A., Loumagne, C., Baup, F., El Hajj, M., Garrigues, S., 2011. Analysis of TerraSAR-X data sensitivity to bare soil moisture, roughness, composition and soil crust. Remote Sensing of Environment 115, 1801–1810. doi:10.1016/j.rse.2011.02.021

Baghdadi, N., Abou Chaaya, J., Zribi, M., 2011. Semiempirical calibration of the integral equation model for SAR data in C-Band and cross polarization using radar images and field measurements. IEEE

689 Geoscience and Remote Sensing Letters 8, 14–18. doi:10.1109/LGRS.2010.2050054

690 Baghdadi, N., Choker, M., Zribi, M., Hajj, M., Paloscia, S., Verhoest, N., Lievens, H., Baup, F., Mattia, F.,
691 2016. A New Empirical Model for Radar Scattering from Bare Soil Surfaces. Remote Sensing 8, 920.
692 doi:10.3390/rs8110920

693 Baghdadi, N., Gaultier, S., King, C., 2002a. Retrieving surface roughness and soil moisture from synthetic
694 aperture radar (SAR) data using neural networks. Canadian Journal of Remote Sensing.
695 doi:10.5589/m02-066

696 Baghdadi, N., Gherboudj, I., Zribi, M., Sahebi, M., King, C., Bonn, F., 2004. Semi-empirical calibration of
697 the IEM backscattering model using radar images and moisture and roughness field measurements.
698 International Journal of Remote Sensing 25, 3593–3623. doi:10.1080/01431160310001654392

699 Baghdadi, N., Holah, N., Zribi, M., 2006. Soil moisture estimation using multi-incidence and multi-
700 polarization ASAR data. International Journal of Remote Sensing. doi:10.1080/01431160500239032

701 Baghdadi, N., King, C., Chanzy, A., Wigneron, J.P., 2002b. An empirical calibration of the integral
702 equation model based on SAR data, soil moisture and surface roughness measurement over bare soils.
703 International Journal of Remote Sensing 23, 4325–4340. doi:10.1080/01431160110107671

704 Baghdadi, N., Zribi, M., 2006. Evaluation of radar backscatter models IEM, OH and Dubois using
705 experimental observations. International Journal of Remote Sensing 27, 3831–3852.
706 doi:10.1080/01431160600658123

707 Baghdadi, N., Zribi, M., Loumagne, C., Ansart, P., Anguela, T.P., 2008. Analysis of TerraSAR-X data and
708 their sensitivity to soil surface parameters over bare agricultural fields. Remote Sensing of
709 Environment. doi:10.1016/j.rse.2008.08.004

710 Baghdadi, Holah, N., Zribi, M., 2006. Soil moisture estimation using multi-incidence and multi-polarization
711 ASAR data. International Journal of Remote Sensing 27, 1907–1920.
712 doi:10.1080/01431160500239032

713 Bai, X., He, B., Li, X., Zeng, J., Wang, X., Wang, Z., Zeng, Y., Su, Z., 2017. First assessment of Sentinel-
714 1A data for surface soil moisture estimations using a coupled water cloud model and advanced integral
715 equation model over the Tibetan Plateau. Remote Sensing. doi:10.3390/rs9070714

716 Bastiaanssen, W.G.M., Menenti, M., Feddes, R.A., Holtslag, A.A.M., 1998. A remote sensing surface
717 energy balance algorithm for land (SEBAL). Journal of Hydrology. doi:10.1016/S0022-
718 1694(98)00253-4

719 Batra, N., Islam, S., Venturini, V., Bisht, G., Jiang, L., 2006. Estimation and comparison of
720 evapotranspiration from MODIS and AVHRR sensors for clear sky days over the Southern Great
721 Plains. Remote Sensing of Environment. doi:10.1016/j.rse.2006.02.019

722 Berk, A., Anderson, G.P., Acharya, P.K., Bernstein, L.S., Muratov, L., Lee, J., Fox, M., Adler-Golden,
723 S.M., Chetwynd, J.H., Hoke, M.L., Lockwood, R.B., Gardner, J.A., Cooley, T.W., Borel, C.C., Lewis,
724 P.E., 2005. MODTRAN 5: a reformulated atmospheric band model with auxiliary species and practical
725 multiple scattering options: update 5806, 662. doi:10.1117/12.606026

726 Boisvert, J.B., Gwyn, Q.H.J., Chanzy, A., Major, D.J., Brisco, B., Brown, R.J., 1997. Effect of surface soil
727 moisture gradients on modelling radar backscattering from bare fields. Int. J. Remote Sens. 18, 153–
728 170. doi:10.1080/014311697219330

729 Brisson, Perrier, 1991. A semi-empirical model of bare soil evaporation for crop simulation models. Water
730 resources 27, 719–727.

731 Bruckler, L., Witono, H., Stengel, P., 1988. Near surface soil moisture estimation from microwave
732 measurements. Remote Sensing of Environment. doi:10.1016/0034-4257(88)90091-0

733 Brutsaert, W., 1975. On a derivable formula for long???wave radiation from clear skies. Water Resources
734 Research. doi:10.1029/WR011i005p00742

735 Budyko, M.I., 1956. Heat balance of the Earth's surface. Gidrometeoizdat, Leningrad. Cahill, 255.

736 Carlson, T., 2007. An Overview of the "Triangle Method" for Estimating Surface Evapotranspiration and
737 Soil Moisture from Satellite Imagery. Sensors. doi:10.3390/s7081612

738 Carlson, T.N., Gillies, R.R., Schmugge, T.J., 1995. An interpretation of methodologies for indirect
739 measurement of soil water content. Agricultural and Forest Meteorology 77, 191–205.
740 doi:10.1016/0168-1923(95)02261-U

741 Champion, I., Faivre, R., 1997. Sensitivity of the radar signal to soil moisture: variation with incidence
742 angle, frequency, and polarization. IEEE Transactions on Geoscience and Remote Sensing.
743 doi:10.1109/36.582001

744 Chanzy, A., 1993. Basic soil surface characteristics derived from active microwave remote sensing. Remote
745 Sensing Reviews.

746 Chanzy, A., 1991. Modélisation simplifiée de l'évaporation d'un sol nu utilisant l'humidité et la
747 température de surface accessibles par télédétection. Institut national agronomique Paris-Grignon.

748 Chanzy, A., Bruckler, L., 1993. Significance of soil surface moisture with respect to daily bare soil

749 evaporation. Water Resources Research. doi:10.1029/92WR02747

750 Chauhan, S., Srivastava, H.S., 2016. Comparative Evaluation of the Sensitivity of Multi-Polarised Sar and
751 Optical Data for Various Land Cover. International Journal of Advancement in Remote Sensing, GIS
752 and Geography COMPARATIVE 4, 1–14.

753 Chehbouni, A.H., Escadafal, R., Duchemin, B., Boulet, G., Simonneaux, V., Dedieu, G., Mougenot, B.,
754 Khabba, S., Kharrou, H., Maisongrande, P., Merlin, O., Chaponnière, A., Ezzahar, J., Er-Raki, S.,
755 Hoedjes, J., Hadria, R., Abourida, A., Cheggour, A., Raibi, F., Boudhar, A., Benhadj, I., Hanich, L.,
756 Benkaddour, A., Guemouria, N., Chehbouni, A.H., Lahrouni, A., Olioso, A., Jacob, F., Williams,
757 D.G., Sobrino, J.A., 2008. An integrated modelling and remote sensing approach for hydrological
758 study in arid and semi-arid regions: the SUDMED Programme. International Journal of Remote
759 Sensing 29, 5161–5181. doi:10.1080/01431160802036417

760 Choi, M., Kim, T.A.E.W., Kustas, W.P., 2011. Reliable estimation of evapotranspiration on agricultural
761 fields predicted by the Priestley – Taylor model using soil moisture data from ground and remote
762 sensing observations compared with the Common Land Model 32, 4571–4587.
763 doi:10.1080/01431161.2010.489065

764 Cosby, B.J., Hornberger, G.M., Clapp, R.B., Ginn, T.R., 1984. A Statistical Exploration of the
765 Relationships of Soil Moisture Characteristics to the Physical Properties of Soils. Water Resources
766 Research 20, 682–690. doi:10.1029/WR020i006p00682

767 Dee, D., Uppala, S., Simmons, a., Berrisford, P., Poli, P., Kobayashi, S., Andrae, U., Balmaseda, M.,
768 Balsamo, G., Bauer, P., 2011. The ERA - Interim reanalysis: Configuration and performance of the
769 data assimilation system. Quaterly Journal of the Royal Meteorological Society. doi:10.1002/qj.828

770 Desborough, C.E., Pitman, A.J., Irannejad, P., 1996. Analysis of the relationship between bare soil
771 evaporation and soil moisture simulated by 13 land surface schemes for a simple non-vegetated site.
772 Global and Planetary Change. doi:10.1016/0921-8181(95)00036-4

773 Dobson, M.C., Ulaby, F., 1981. Microwave Backscatter Dependence on Surface Roughness, Soil Moisture,
774 and Soil Texture: Part III—Soil Tension. IEEE Transactions on Geoscience and Remote Sensing.
775 doi:10.1109/TGRS.1981.350328

776 Dobson, M.C., Ulaby, F.T., 1986. Active Microwave Soil Moisture Research. IEEE Transactions on
777 Geoscience and Remote Sensing. doi:10.1109/TGRS.1986.289585

778 Dobson, M.C., Ulaby, F.T., Hallikainen, M.T., El-Rayes, M.A., 1985. Microwave Dielectric Behavior of
779 Wet Soil-Part II: Dielectric Mixing Models. IEEE Transactions on Geoscience and Remote Sensing.

780 doi:10.1109/TGRS.1985.289498

781 Du, Y., Ulaby, F.T., Dobson, M.C., 2000. Sensitivity to soil moisture by active and passive microwave
782 sensors. Geoscience and Remote Sensing, IEEE Transactions on.

783 Dubois, P.C., Engman, T., 1995a. Measuring Soil Moisture with Imaging Radars. IEEE Transactions on
784 Geoscience and Remote Sensing. doi:10.1109/36.406677

785 Dubois, P.C., Engman, T., 1995b. Measuring Soil Moisture with Imaging Radars. IEEE Transactions on
786 Geoscience and Remote Sensing 33, 915–926. doi:10.1109/36.406677

787 Duchemin, B., Hadria, R., Erraki, S., Boulet, G., Maisongrande, P., Chehbouni, A., Escadafal, R., Ezzahar,
788 J., Hoedjes, J.C.B., Kharrou, M.H., Khabba, S., Mougenot, B., Olioso, A., Rodriguez, J.C.,
789 Simonneaux, V., 2006. Monitoring wheat phenology and irrigation in Central Morocco: On the use of
790 relationships between evapotranspiration, crops coefficients, leaf area index and remotely-sensed
791 vegetation indices. Agricultural Water Management. doi:10.1016/j.agwat.2005.02.013

792 Engman, E.T., 2000. Soil moisture., Ed. G.A. Schultz, E.T. Engman, . Berlin: Springer Grayson,. Remote
793 sensing in hydrology and water management 197–216.

794 Entekhabi, D., Njoku, E.G., O'Neill, P.E., Kellogg, K.H., Crow, W.T., Edelstein, W.N., Entin, J.K.,
795 Goodman, S.D., Jackson, T.J., Johnson, J., Kimball, J., Piepmeier, J.R., Koster, R.D., Martin, N.,
796 McDonald, K.C., Moghaddam, M., Moran, S., Reichle, R., Shi, J.C., Spencer, M.W., Thurman, S.W.,
797 Tsang, L., Van Zyl, J., 2010. The soil moisture active passive (SMAP) mission. Proceedings of the
798 IEEE. doi:10.1109/JPROC.2010.2043918

799 Entekhabi, D., Rodriguez-Iturbe, I., Castelli, F., 1996. Mutual interaction of soil moisture state and
800 atmospheric processes. Journal of Hydrology. doi:10.1016/0022-1694(95)02965-6

801 Er-Raki, S., Chehbouni, A., Guemouria, N., Duchemin, B., Ezzahar, J., Hadria, R., 2007. Combining FAO-
802 56 model and ground-based remote sensing to estimate water consumptions of wheat crops in a semi-
803 arid region. Agricultural Water Management 87, 41–54. doi:10.1016/j.agwat.2006.02.004

804 Eweys, O.A., Elwan, A., Borham, T., 2017. Retrieving topsoil moisture using RADARSAT-2 data, a novel
805 approach applied at the east of the Netherlands. Journal of Hydrology, In review 555, 670–682.
806 doi:10.1016/j.jhydrol.2017.10.048

807 Fieuzal, R., 2010. Interactive comment on " Combined use of optical and radar satellite data for the
808 monitoring of irrigation and soil moisture of wheat crops " by 7–9.

809 Fieuzal, R., Duchemin, B., Jarlan, L., Zribi, M., Baup, F., Merlin, O., Hagolle, O., Garatuza-Payan, J., 2011.

Combined use of optical and radar satellite data for the monitoring of irrigation and soil moisture of wheat crops. Hydrology and Earth System Sciences 15, 1117–1129. doi:10.5194/hess-15-1117-2011

Friedl, M.A., Davis, F.W., 1994. Sources of variation in radiometric surface temperature over a tallgrass prairie. Remote Sensing of Environment 48, 1–17. doi:10.1016/0034-4257(94)90109-0

Fung, A.K., 1994. Microwave scattering and emission models and their applications. Artech House Remote Sensing Library.

Fung, A.K., Li, Z., Chen, K.S., 1992. Backscattering from a Randomly Rough Dielectric Surface. IEEE Transactions on Geoscience and Remote Sensing. doi:10.1109/36.134085

Gao, Q., Zribi, M., Escorihuela, M., Baghdadi, N., 2017. Synergetic Use of Sentinel-1 and Sentinel-2 Data for Soil Moisture Mapping at 100 m Resolution. Sensors 17, 1966. doi:10.3390/s17091966

Gherboudj, I., Magagi, R., Berg, A.A., Toth, B., 2011. Soil moisture retrieval over agricultural fields from multi-polarized and multi-angular RADARSAT-2 SAR data. Remote Sensing of Environment 115, 33–43. doi:10.1016/j.rse.2010.07.011

Gillies, R.R., Carlson, T.N., 1995. Thermal Remote-Sensing of Surface Soil-Water Content with Partial Vegetation Cover for Incorporation into Climate-Models. Journal of Applied Meteorology. doi:10.1175/1520-0450(1995)034<0745:trsoss>2.0.co;2

Goward, S.N., Tucker, C.J., Dye, D.G., 1985. North American vegetation patterns observed with the NOAA-7 advanced very high resolution radiometer. Vegetatio. doi:{10.1007/BF00033449}

Hadria, R., Duchemin, B., Lahrouni, A., Khabba, S., Er-raki, S., Dedieu, G., Chehbouni, A.G., Olioso§, A., 2006. Monitoring of irrigated wheat in a semi-arid climate using crop modelling and remote sensing data: Impact of satellite revisit time frequency. International Journal of Remote Sensing 27, 1093–1117. doi:10.1080/01431160500382980

Holah, N., Baghdadi, N., Zribi, M., Bruand, A., King, C., 2005a. Potential of ASAR / ENVISAT for the characterization of soil surface parameters over bare agricultural fields 96, 78–86. doi:10.1016/j.rse.2005.01.008

Holah, N., Baghdadi, N., Zribi, M., Bruand, A., King, C., 2005b. Potential of ASAR/ENVISAT for the characterization of soil surface parameters over bare agricultural fields. Remote Sensing of Environment 96, 78–86. doi:10.1016/j.rse.2005.01.008

Jackson, R.D.., Pinter, P.J., 1981. Detection of Water Stress in Wheat by Measurement of Reflected Solar and Emitted Thermal IR Radiation. In Spectral Signatures of Objects in Remote Sensing. Institute

National de la Recherche Agronomique: Versailles, France 399–406.

Jarlan, L., Khabba, S., Er-Raki, S., Le Page, M., Hanich, L., Fakir, Y., Merlin, O., Mangiarotti, S., Gascoin, S., Ezzahar, J., Kharrou, M.H., Berjamy, B., Saaïdi, A., Boudhar, A., Benkaddour, A., Laftouhi, N., Abaoui, J., Tavernier, A., Boulet, G., Simonneaux, V., Driouech, F., El Adnani, M., El Fazziki, A., Amenzou, N., Raibi, F., El Mandour, A., Ibouh, H., Le Dantec, V., Habets, F., Tramblay, Y., Mougenot, B., Leblanc, M., El Faïz, M., Drapeau, L., Coudert, B., Hagolle, O., Filali, N., Belaqziz, S., Marchane, A., Szczypta, C., Toumi, J., Diarra, A., Aouade, G., Hajhouji, Y., Nassah, H., Bigeard, G., Chirouze, J., Boukhari, K., Abourida, A., Richard, B., Fanise, P., Kasbani, M., Chakir, A., Zribi, M., Marah, H., Naimi, A., Mokssit, A., Kerr, Y., Escadafal, R., 2015. Remote Sensing of Water Resources in Semi-Arid Mediterranean Areas: the joint international laboratory TREMA. International Journal of Remote Sensing. doi:10.1080/01431161.2015.1093198

Julien, Y., Sobrino, J.A., 2009. The Yearly Land Cover Dynamics (YLCD) method: An analysis of global vegetation from NDVI and LST parameters. Remote Sensing of Environment. doi:10.1016/j.rse.2008.09.016

Karam, M.A., Fung, A.K., Lang, R.H., Chauhan, N.S., 1992. Microwave Scattering Model for Layered Vegetation. IEEE Transactions on Geoscience and Remote Sensing. doi:10.1109/36.158872

Karjalainen, M., Harri, K., Hyyppä, J., Laurila, H., Kuittinen, R., 2014. the Use of Envisat Alternating Polarization Sar Images in Agricultural Monitoring in Comparison With Radarsat-1 Sar Images. In Proceedings of the ISPRS Congress, Istanbul, Turkey.

Kerr, Y.H., Waldteufel, P., Wigneron, J.P., Delwart, S., Cabot, F., Boutin, J., Escorihuela, M.J., Font, J., Reul, N., Gruhier, C., Juglea, S.E., Drinkwater, M.R., Hahne, A., Martin-Neira, M., Mecklenburg, S., 2010. The SMOS Mission: New Tool for Monitoring Key Elements of the Global Water Cycle. Proceedings of the Ieee. doi:10.1109/jproc.2010.2043032

Khabba, S., Jarlan, L., Er-Raki, S., Page, M. Le, Ezzahar, J., Boulet, G., Simonneaux, V., Kharrou, M.H., Hanich, L., Chehbouni, G., 2013. The SudMed Program and the Joint International Laboratory TREMA: A Decade of Water Transfer Study in the Soil-Plant-Atmosphere System over Irrigated Crops in Semi-Arid Area. Procedia Environmental Sciences 19, 524–33.

Kharrou, M.H., Le Page, M., Chehbouni, A., Simonneaux, V., Er-Raki, S., Jarlan, L., Ouzine, L., Khabba, S., Chehbouni, G., 2013. Assessment of Equity and Adequacy of Water Delivery in Irrigation Systems Using Remote Sensing-Based Indicators in Semi-Arid Region, Morocco. Water Resources Management. doi:10.1007/s11269-013-0438-5

871 Kim, J., Hogue, T.S., 2012. Improving spatial soil moisture representation through integration of AMSR-
872 E and MODIS products. IEEE Transactions on Geoscience and Remote Sensing.
873 doi:10.1109/TGRS.2011.2161318

874 Lagouarde, J.P., Dayau, S., Moreau, P., Guyon, D., 2014. Directional anisotropy of brightness surface
875 temperature over vineyards: Case study over the Medoc Region (SW France). IEEE Geoscience and
876 Remote Sensing Letters. doi:10.1109/LGRS.2013.2282492

877 Le H??garat-Mascle, S., Zribi, M., Alem, F., Weisse, A., Loumagne, C., 2002. Soil moisture estimation
878 from ERS/SAR data: Toward an operational methodology. IEEE Transactions on Geoscience and
879 Remote Sensing. doi:10.1109/TGRS.2002.806994

880 Le Hégarat, S., Zribi, M., Alem, F., Weisse, A., Loumagne, C., 2002. Soil moisture estimation from
881 ERS/SAR data: Toward an operational methodology. IEEE Transactions on Geoscience and Remote
882 Sensing. doi:10.1109/TGRS.2002.806994

883 Le Morvan, A., Zribi, M., Baghdadi, N., Chanzy, A., 2008. Soil Moisture Profile Effect on Radar Signal
884 Measurement. Sensors 8, 256–270. doi:10.3390/s8010256

885 Lee, J.S., Jurkevich, L., Dewaele, P., Wambacq, P., Oosterlinck, A., 1994. Speckle filtering of synthetic
886 aperture radar images: A review. Remote Sensing Reviews. doi:10.1080/02757259409532206

887 Lee, J. Sen, 1999. Polarimetric SAR speckle filtering and its implication for classification. IEEE
888 Transactions on Geoscience and Remote Sensing. doi:10.1109/36.789635

889 Lievens, H., Verhoest, N.E.C., 2011. On the Retrieval of Soil Moisture in Wheat Fields From L-Band SAR
890 Based on Water Cloud Modeling, the IEM, and Effective Roughness Parameters. IEEE Geoscience
891 and Remote Sensing Letters 8, 740–744. doi:10.1109/LGRS.2011.2106109

892 Loew, A., Ludwig, R., Mauser, W., 2006. Derivation of surface soil moisture from ENVISAT ASAR wide
893 swath and image mode data in agricultural areas. IEEE Transactions on Geoscience and Remote
894 Sensing. doi:10.1109/TGRS.2005.863858

895 Mahfouf, J.-F., Noilhan, J., 1996. Inclusion of Gravitational Drainage in a Land Surface Scheme Based on
896 the Force-Restore Method. Journal of Applied Meteorology 35, 987–992. doi:10.1175/1520-
897 0450(1996)035<0987:IOGDIA>2.0.CO;2

898 Mahfouf J.-F., Noilhan, J., 1991. Comparative Study of Various Formulations of Evaporation from Bare
899 Soil Using In Situ Data. Journal of Applied Meteorology.

900 Manabe, S., 1969. Climate and the Ocean Circulation I. The Atmospheric Circulation and the Hydrology

of the Earth's Surface. Monthly Weather Review. doi:10.1175/1520-0493(1969)097<0739:CATOC>2.3.CO;2

Mathieu, R., Sbih, M., Viau, A.A., Anctil, F., Parent, L.E., Boisvert, J., 2003. {R}elationships between {R}adarsat {SAR} data and surface moisture content of agricultural organic soils. INTERNATIONAL JOURNAL OF REMOTE SENSING. doi:10.1080/0143116031000115247

Mattar, C., Wigneron, J.P., Sobrino, J.A., Novello, N., Calvet, J.C., Albergel, C., Richaume, P., Mialon, A., Guyon, D., Jimenez-Munoz, J.C., Kerr, Y., 2012. A combined optical-microwave method to retrieve soil moisture over vegetated areas. IEEE Transactions on Geoscience and Remote Sensing 50, 1404–1413. doi:10.1109/TGRS.2011.2179051

McVicar, T.R.., Jupp, D.B.., Yang, X., 1992. Linking Regional Water Balance Models with Remote Sensing. In Proceedings of the 13th Asian Conference on Remote Sensing, Ulaanbaatar, Mongolia.

Merlin, O., 2013. An original interpretation of the wet edge of the surface temperature-albedo space to estimate crop evapotranspiration (SEB-1S), and its validation over an irrigated area in northwestern Mexico. Hydrology and Earth System Sciences 17, 3623–3637. doi:10.5194/hess-17-3623-2013

Merlin, O., Olivera-guerra, L., Bouchra, A.H., Amazirh, A., Rafi, Z., Ezzahar, J., Gentine, P., Khabba, S., Gascoin, S., Er-raki, S., 2017. A phenomenological model of soil evaporative efficiency using readily available data. Agricultural and Forest Meteorology, In review.

Merlin, O., Stefan, V.G., Amazirh, A., Chanzy, A., Ceschia, E., Tallec, T., Beringer, J., Gentine, P., Er-Raki, S., Bircher, S., Khabba, S., 2016. Modeling soil evaporation efficiency in a range of soil and atmospheric conditions: A downward approach based on multi-site data. Submitted to Water Resources Research.

Merlin, O., Walker, J.P., Chehbouni, A., Kerr, Y., 2008. Towards deterministic downscaling of SMOS soil moisture using MODIS derived soil evaporative efficiency. Remote Sensing of Environment. doi:10.1016/j.rse.2008.06.012

Molero, B., Merlin, O., Malbéteau, Y., Bitar, A. Al, Cabot, F., Stefan, V., Kerr, Y., Bacon, S., Cosh, M.H., Bindlish, R., Jackson, T.J., 2016. Remote Sensing of Environment SMOS disaggregated soil moisture product at 1 km resolution : Processor overview and fi rst validation results. Remote Sensing of Environment. doi:10.1016/j.rse.2016.02.045

Moran, M.S., Clarke, T.R., Inoue, Y., Vidal, A., 1994. Estimating crop water deficit using the relation between surface-air temperature and spectral vegetation index. Remote Sensing of Environment. doi:10.1016/0034-4257(94)90020-5

Moran, M.S., Jackson, R.D., Slater, P.N., Teillet, P.M., 1992. Evaluation of simplified procedures for retrieval of land surface reflectance factors from satellite sensor output. Remote Sensing of Environment. doi:10.1016/0034-4257(92)90076-V

Nemani, R.R., Running, S.W., 1989. Estimation of regional surface resistance to evapotranspiration from NDVI and thermal-IR AVHRR data. Journal of Applied Meteorology. doi:10.1175/1520-0450(1989)028<0276:EORSRT>2.0.CO;2

Nishida, K., Nemani, R.R., Glassy, J.M., Running, S.W., 2003. Development of an evapotranspiration index from Aqua/MODIS for monitoring surface moisture status. IEEE Transactions on Geoscience and Remote Sensing. doi:10.1109/TGRS.2003.811744

Oh, Y., 2004. Quantitative retrieval of soil moisture content and surface roughness from multipolarized radar observations of bare soil surfaces. IEEE Transactions on Geoscience and Remote Sensing. doi:10.1109/TGRS.2003.821065

Oh, Y., Sarabandi, K., Ulaby, F.T., 1992. An empirical model and an inversion technique for radar scattering from bare soil surfaces. IEEE Transactions on Geoscience and Remote Sensing. doi:10.1109/36.134086

Omer, S.K., Bitar, A. Al, Sekhar, M., Zribi, M., Bandyopadhyay, S., 2015. Retrieval and Multi-scale Validation of Soil Moisture from 8128–8153. doi:10.3390/rs70608128

Peng, J., Loew, A., Merlin, O., Verhoest, N.E.C., 2017. A review of spatial downscaling of satellite remotely-sensed soil moisture. Submitted to Reviews of Geophysics. doi:10.1002/2016RG000543

Price, J.C., 1990. Using spatial context in satellite data to infer regional scale evapotranspiration. IEEE Transactions on Geoscience and Remote Sensing. doi:10.1109/36.58983

Qin, J., Yang, K., Lu, N., Chen, Y., Zhao, L., Han, M., 2013. Spatial upscaling of in-situ soil moisture measurements based on MODIS-derived apparent thermal inertia. Remote Sensing of Environment. doi:10.1016/j.rse.2013.07.003

Quesney, A., Le Hégarat-Mascle, S., Taconet, O., Vidal-Madjar, D., Wigneron, J.P., Loumagne, C., Normand, M., 2000. Estimation of watershed soil moisture index from ERS/SAR data. Remote Sensing of Environment. doi:10.1016/S0034-4257(99)00102-9

Rakotoarivony L., O. Taconet, Vidal-Madjar, D., 1996. Radar backscattering over agricultural bare soils. Journal of Electromagnetic Waves and Applications.

Remond, A., Beaudoin, A., King, C., 1999. SAR imagery to estimate roughness parameters when modelling

runoff risk. International Journal of Remote Sensing. doi:10.1080/014311699211967

Roerink, G.J., Su, Z., Menenti, M., 2000. S-SEBI: A simple remote sensing algorithm to estimate the surface energy balance. Physics and Chemistry of the Earth Part B-Hydrology Oceans and Atmosphere.

Sandholt, I., Rasmussen, K., Andersen, J., 2002. A simple interpretation of the surface temperature/vegetation index space for assessment of surface moisture status. Remote Sensing of Environment 79, 213–224. doi:10.1016/S0034-4257(01)00274-7

Santamaria-Artigas, A., Mattar, C., Wigneron, J.P., 2016. Application of a Combined Optical-Passive Microwave Method to Retrieve Soil Moisture at Regional Scale over Chile. IEEE Journal of Selected Topics in Applied Earth Observations and Remote Sensing 9, 1493–1504. doi:10.1109/JSTARS.2015.2512926

Schmugge, T., 1978. Remote sensing of surface soil moisture. Design. doi:10.1029/JC080i021p03044

Shi, J., Wang, J., Hsu, A.Y., O'Neill, P.E., Engman, E.T., 1997. Estimation of bare surface soil moisture and surface roughness parameter using L-band SAR image data. IEEE Transactions on Geoscience and Remote Sensing. doi:10.1109/36.628792

Smith, R.C.G., Choudhury, B.J., 1991. Analysis of normalized difference and surface temperature observations over southeastern Australia. Remote Sensing. doi:10.1080/01431169108955234

Sobrino, J.A., Franch, B., Mattar, C., Jiménez-Muñoz, J.C., Corbari, C., 2012. A method to estimate soil moisture from Airborne Hyperspectral Scanner (AHS) and ASTER data: Application to SEN2FLEX and SEN3EXP campaigns. Remote Sensing of Environment. doi:10.1016/j.rse.2011.10.018

Srivastava, H.S., 2007. Development and Validation of an Improved Methodology for Operational Monitoring of Soil Moisture Over Large Agricultural Area Using Multi- Incidence Angle Radarsat-1 Sar Data and M ...

Srivastava, H.S., Patel, P., Manchanda, M.L., Adiga, S., 2003. Use of multiincidence angle RADARSAT-1 SAR data to incorporate the effect of surface roughness in soil moisture estimation, in: IEEE Transactions on Geoscience and Remote Sensing. doi:10.1109/TGRS.2003.813356

Srivastava, H.S., Patel, P., Sharma, Y., Navalgund, R.R., 2009. Large-Area Soil Moisture Estimation Using 47, 2528–2535.

Srivastava, H.S., Patel, P., Sharma, Y., Navalgund, R.R., 2008. Retrieval of surface roughness using multi-polarized Envisat-1 ASAR data. Geocarto International 23, 67–77. doi:10.1080/10106040701538157

992 Stefan, V.G., Merlin, O., Er-Raki, S., Escorihuela, M.J., Khabba, S., 2015. Consistency between In Situ,
993 model-derived and high-resolution-image-based soil temperature endmembers: Towards a robust data-
994 based model for multi-resolution monitoring of crop evapotranspiration. Remote Sensing.
995 doi:10.3390/rs70810444

996 Susaki, J., 2008. CALIBRATION OF IEM MODEL FOR THE SOIL MOISTURE MAPPING OF NON-
997 INUNDATED PADDY FIELDS USING ALOS / PALSAR DATA Junichi Susaki Graduate School
998 of Global Environmental Studies ,. Sites The Journal Of 20Th Century Contemporary French Studies
999 753–756.

1000 Tardy, B., Rivalland, V., Huc, M., Hagolle, O., Marcq, S., Boulet, G., 2016. A Software Tool for
1001 Atmospheric Correction and Surface Temperature Estimation of Landsat Infrared Thermal Data 1–24.
1002 doi:10.3390/rs8090696

1003 Torres, R., Snoeij, P., Geudtner, D., Bibby, D., Davidson, M., Attema, E., Potin, P., Rommen, B. ??rn,
1004 Floury, N., Brown, M., Traver, I.N., Deghaye, P., Duesmann, B., Rosich, B., Miranda, N., Bruno, C.,
1005 L'Abbate, M., Croci, R., Pietropaolo, A., Huchler, M., Rostan, F., 2012. GMES Sentinel-1 mission.
1006 Remote Sensing of Environment. doi:10.1016/j.rse.2011.05.028

1007 Ulaby, F.T., Batlivala, P.P., Dobson, M.C., 1978. Microwave Backscatter Dependence on Surface
1008 Roughness, Soil Moisture, and Soil Texture: Part I–Bare Soil. IEEE Transactions on Geoscience
1009 Electronics. doi:10.1109/TGE.1978.294586

1010 Ulaby, F.T., Bradley, G.A., Obson, M.C., 1979. Microwave Backscatter Dependence on Surface
1011 Roughness, Soil Moisture, and Soil Texture: Part II–Vegetation-Covered Soil. IEEE Transactions on
1012 Geoscience Electronics. doi:10.1109/TGE.1979.294626

1013 Ulaby, F.T., Moore, R.K., Fung, A.K., 1986. Microwave remote sensing: Active and passive. Volume 3 -
1014 From theory to applications, Microwave Remote Sensing Active and Passive.

1015 Van Oevelen, P.J., Hoekman, D.H., 1999. Radar backscatter inversion techniques for estimation of surface
1016 soil moisture: EFEDA-spain and HAPEX-SAHEL case studies. IEEE Transactions on Geoscience and
1017 Remote Sensing. doi:10.1109/36.739141

1018 Vereecken, H., Huisman, J.A., Bogena, H., Vanderborght, J., Vrugt, J.A., Hopmans, J.W., 2008. On the
1019 value of soil moisture measurements in vadose zone hydrology : A review 44, 1–21.
1020 doi:10.1029/2008WR006829

1021 Verstraeten, W.W., Veroustraete, F., Feyen, J., 2008. Assessment of Evapotranspiration and Soil Moisture
1022 Content Across Different Scales of Observation 70–117.

Wagner, W., Lemoine, G., Borgeaud, M., Member, S., Rott, H., 1999a. A Study of Vegetation Cover Effects on ERS Scatterometer Data 37, 938–948.

Wagner, W., Lemoine, G., Rott, H., 1999b. A Method for Estimating Soil Moisture from ERS Scatterometer and Soil Data. Remote Sensing of Environment 4257.

Wan, Z., Wang, P., Li, X., 2004. Using MODIS Land Surface Temperature and Normalized Difference Vegetation Index products for monitoring drought in the southern Great Plains, USA. International Journal of Remote Sensing. doi:10.1080/0143116031000115328

Wang, K., Li, Z., Cribb, M., 2006. Estimation of evaporative fraction from a combination of day and night land surface temperatures and NDVI: A new method to determine the Priestley-Taylor parameter. Remote Sensing of Environment. doi:10.1016/j.rse.2006.02.007

Wickel, A.J., Jackson, T.J., Wood, E.F., 2001. Multi-temporal monitoring of soil moisture with RADARSAT SAR during the 1997 Southern Great Plains hydrology experiment. International Journal of Remote Sensing. doi:10.1080/01431160120291

Zhang, D., Zhou, G., 2016. Estimation of Soil Moisture from Optical and Thermal Remote Sensing : A Review. doi:10.3390/s16081308

Zhang, F., Zhang, L.W., Shi, J.J., Huang, J.F., 2014. Soil moisture monitoring based on land surface temperature-vegetation index space derived from MODIS data. Pedosphere 24, 450–460. doi:10.1016/S1002-0160(14)60031-X

Zribi, M., André, C., Decharme, B., 2008. A method for soil moisture estimation in Western Africa based on the ERS scatterometer, in: IEEE Transactions on Geoscience and Remote Sensing. doi:10.1109/TGRS.2007.904582

Zribi, M., Baghdadi, N., Holah, N., Fafin, O., 2005. New methodology for soil surface moisture estimation and its application to ENVISAT-ASAR multi-incidence data inversion. Remote Sensing of Environment. doi:10.1016/j.rse.2005.04.005

Zribi, M., Chahbi, A., Shabou, M., Duchemin, B., Baghdadi, N., Amri, R., 2011. Soil surface moisture estimation over a semi-arid region using ENVISAT ASAR radar data for soil evaporation evaluation 345–358. doi:10.5194/hess-15-345-2011

Zribi, M., Dechambre, M., 2003. A new empirical model to retrieve soil moisture and roughness from C-band radar data. Remote Sensing of Environment 84, 42–52. doi:10.1016/S0034-4257(02)00069-X

Zribi, M., Taconet, O., H??garat-Mascle, S. Le, Vidal-Madjar, D., Emblanch, C., Loumagne, C., Normand,

M., 1997. Backscattering behavior and simulation comparison over bare soils using SIR-C/X-SAR and ERASME 1994 data over Orgeval. Remote Sensing of Environment. doi:10.1016/S0034-4257(96)00158-7